UNIVERSIDADE FEDERAL DO CEARÁ
CENTRO DE TECNOLOGIA
DEPARTAMENTO DE ENGENHARIA METALÚRGICA E DE MATERIAIS
PROGRAMA DE PÓS-GRADUAÇÃO EM ENGENHARIA E CIÊNCIA DE MATERIAIS

MILLIANE PASSOS DA SILVA PALÁCIO

DUAL SPECTRAL MATCHING IN PEROVSKITE SOLAR CELLS VIA UPCONVERTING PLUS DOWNSHIFTING NANOPARTICLES

FORTALEZA
2025

MILLIANE PASSOS DA SILVA PALÁCIO

DUAL SPECTRAL MATCHING IN PEROVSKITE SOLAR CELLS VIA UPCONVERTING PLUS DOWNSHIFTING NANOPARTICLES

Doctoral Thesis submitted to the Graduate Program in Materials Science and Engineering at the Federal University of Ceará in partial fulfillment of the requirements for the degree of Doctor in Materials Science and Engineering. Concentration area: Physical and Mechanical Properties of Materials.

Advisor: Prof. Dr. Igor Frota de Vasconcelos
Co-Advisor: Prof. Dr. Luís Paulo Mourão dos Santos
Co-Advisor (stay at Portugal): Prof. Dr. Maria Rute de Amorim e Sá Ferreira André

FORTALEZA

2025

Dados Internacionais de Catalogação na Publicação
Universidade Federal do Ceará
Sistema de Bibliotecas
Gerada automaticamente pelo módulo Catalog, mediante os dados fornecidos pelo(a) autor(a)

P176d Palácio, Milliane Passos da Silva.
Dual spectral matching in perovskite solar cells via upconverting plus downshifiting nanoparticles / Milliane Passos da Silva Palácio. – 2025.
72 f. : il. color.

Tese (doutorado) – Universidade Federal do Ceará, Centro de Tecnologia, Programa de Pós-Graduação em Engenharia e Ciência de Materiais, Fortaleza, 2025.
Orientação: Prof. Dr. Igor Frota de Vasconcelos.
Coorientação: Prof. Dr. Luís Paulo Mourão dos Santos.

1. spectral conversion. 2. nanoparticles. 3. lanthanides. 4. perovskite solar cells. I. Título.
CDD 620.11

MILLIANE PASSOS DA SILVA PALÁCIO

DUAL SPECTRAL MATCHING IN PEROVSKITE SOLAR CELLS VIA UPCONVERTING PLUS DOWNSHIFTING NANOPARTICLES

Doctoral Thesis submitted to the Graduate Program in Materials Science and Engineering at the Federal University of Ceará in partial fulfillment of the requirements for the degree of Doctor in Materials Science and Engineering. Concentration area: Physical and Mechanical Properties of Materials.

Defense date: November 05, 2025

DEFENSE COMMITTEE

Prof. Dr. Igor Frota de Vasconcelos (Committee President)
Universidade Federal do Ceará (UFC)

Prof. Dr. Luís Paulo Mourão dos Santos
Universidade Federal do Ceará (UFC)

Prof. Dr. Maria Rute de Amorim e Sá Ferreira André
Universidade de Aveiro (UA)

Prof. Dr. Davino Machado Andrade Neto
Universidade Federal do Ceará (UFC)

Prof. Dr. Wagner Ferreira da Silva
Universidade Federal de Alagoas (UFAL)

Prof. Dr. Francisco Eroni Paz dos Santos
Universidade Federal do Piauí (UFPI)

This thesis is dedicated to all those who, like me, believe that education has the power to transform not only people, but also the world. It is especially dedicated to those who persist in science, particularly in Brazil, during challenging times such as the COVID-19 pandemic, when denialism led many to lose faith in scientific research. It is also a tribute to those behind the scenes, our families, who often feel our absence and, even without fully understanding the time we devote to science, support us unconditionally.

ACKNOWLEDGEMENTS

My sincere thanks go to:

First, to God, a source of inspiration, strength, and courage throughout my journey. To me, He is the great scientist and artist of the universe; as scientists, we merely unveil fragments of His creation. I see Him as free of prejudice and full of love, just as Jesus revealed to us.

To my family, the Passos family, especially my mother, Lucilene, and my siblings, Geovana, Álvaro, and Ângela, for their care, respect, and love. I am grateful to my maternal grandparents, Luzia and Francisco, for raising me and loving me as a daughter, and to my uncle and aunt, Marlene and Daniel, and their families, who have always supported me with affection.

To my husband, Igor, and his family, the Palácio family, for their patience and support throughout my academic journey since undergraduate studies. I could have pursued this path alone, but his constant care and love made it easier.

To my friends and colleagues from the UFC Graduate Program, especially those who shared the laboratory with me through both joys and challenges: Anderson, Breno, Gilvane, Guilherme, Inácio, Iran, Lucas, Maurício, Matheus, Nayuca, Nicholas, Nicolas, Raquele, Rubens, Samuel, Tiago, and Vitória, among others. My apologies if I have forgotten anyone.

To the members of my thesis committee: Professors Igor, Luís, Davino, Eroni, Wagner, and Rute. I am especially grateful to my supervisors at UFC, Igor and Luís, for their unwavering guidance and dedication to my professional growth.

To all the professors who have contributed to my academic path, sharing not only knowledge but also values and inspiration that I will carry for life.

To the Federal University of Ceará, which became my second home throughout more than seven years of graduate studies, during both my master's and doctoral programs, a period marked by challenges, growth, and learning. I am also grateful to the Analytical Central Laboratories of Chemistry and Physics for consistently providing access to UV–Vis, photoluminescence, and XRD measurements. In particular, I extend my sincere appreciation to the technician Nádia, from the Chemistry laboratory, for her guidance, support, and the many times she assisted me during the analyses.

To IFCE Campus Tianguá, especially my Physics professors Felipe, Florêncio, Wellington, Josias, and Nadia, who not only taught me Physics but also guided me toward graduate studies at UFC.

To the public policies implemented during the PT (Workers Party) governments: the Bolsa Família program, which supported my mother in raising my sister and me; the expansion of the Federal Institutes, which gave me access to higher education; and the CAPES scholarships during my undergraduate and graduate studies, which sustained my academic path. I am deeply grateful for these initiatives that transformed my life.

To LNNano at CNPEM, for teaching us to produce high-quality nanoparticles and for microscopy measurements (proposal: 20230784). Special thanks to researchers Batista, Luelc, and Olavo.

To Universidade de Campinas - UNICAMP, for supporting nanoparticle synthesis that contributed to this thesis, with special thanks to Nagyla Oliveira, Sérgio Coelho, and Professor Fernando Sigoli.

To Universidade Federal de Alagoas - UFAL, for the photoluminescence measurements used in my qualification, and for training me in the solvothermal synthesis of nanoparticles. I would like to extend special thanks to Leonardo Barros and Professors Wagner Silva and Carlos Jacinto.

To the University of Aveiro (Portugal), where I completed my sandwich doctoral program and further developed my knowledge of optical measurements of nanoparticles. I thank Professor Rute André for her guidance and Dr. Fernando Maturi for his valuable teachings.

To Universidade Nova de Lisboa (Portugal), for enabling me to fabricate my first PSC devices. Special thanks to Professor Manuel for welcoming me and to Dr. Deneb for her generous support.

Finally, to everyone who contributed, directly or indirectly, to this work.

This work was carried out with the support of the Coordination for the Improvement of Higher Education Personnel (CAPES) – Funding Code 001, and FUNCAP, through the sandwich doctoral scholarship (Process ITR-0214-00020.01.00/23).

“I, a universe of atoms, an atom in the universe”.

(Richard Feynman)

ABSTRACT

Maximizing the efficiency of solar cells is a key step toward advancing photovoltaic technologies and fully harnessing the energy conversion potential of sunlight. This study investigates the incorporation of *core–shell* nanoparticles (NPs) $NaGdF_4:Yb^{3+},Tm^{3+}@NaGdF_4:Eu^{3+}$ (TMN) and $NaGdF_4:Yb^{3+},Er^{3+}@NaGdF_4:Eu^{3+}$ (ERN) into perovskite solar cells (PSCs) with the aim of enhancing their power conversion efficiency. The NPs were synthesized via thermal decomposition and characterized using a set of techniques, including photoluminescence spectroscopy, quantum yield measurements, transmission electron microscopy, X-ray diffraction, solar simulator-based efficiency measurements, and external quantum efficiency evaluations. The lanthanide-doped NPs exhibited intense downshifting luminescence and weaker upconversion emission, acting as spectral converters that transform poorly absorbed regions of the solar spectrum into wavelengths usable by the device. Devices containing ERN NPs showed a relative increase of 22.19% in power conversion efficiency, whereas those with TMN NPs exhibited an improvement of 13.23%. These gains are primarily attributed to the efficient downshifting emission of Eu^{3+} and the superior surface passivation provided by the core–shell architecture. Together, these mechanisms suppress recombination losses and optimize charge carrier dynamics. These results highlight the potential of lanthanide-based photon-converting materials to overcome the intrinsic spectral absorption limitations of PSCs, presenting a promising strategy for the development of next-generation photovoltaic technologies.

Keywords: spectral conversion; nanoparticles; lanthanides; perovskite solar cells

RESUMO

A maximização da eficiência de células solares constitui uma etapa fundamental para a revolução das tecnologias fotovoltaicas e para o pleno aproveitamento do potencial de conversão energética da luz. Este estudo investiga a incorporação de nanopartículas (NPs) com arquitetura caroço-casca de $NaGdF_4:Yb^{3+}$,Tm3+@$NaGdF_4:Eu^{3+}$ (TMN) e $NaGdF_4:Yb^{3+}$,Er^{3+}@$NaGdF_4:Eu^{3+}$ (ERN) em células solares de perovskita (CSPs) visando ao aumento da sua eficiência de conversão de potência. As NPs foram sintetizadas via termólise e caracterizadas por um conjunto de técnicas, como espectroscopia de fotoluminescência, medidas de rendimento quântico, microscopia eletrônica de transmissão, difração de raios X, medidas de eficiência de conversão utilizando simulador solar e avaliações de eficiência quântica externa. As NPs dopadas com lantanídeos exibiram intensa luminescência por conversão descendente e uma menor luminescência por conversão ascendente de energia, atuando como conversores espectrais que transformam regiões do espectro solar pouco absorvidas em comprimentos de onda passíveis de aproveitamento pelo dispositivo. Os dispositivos contendo NPs ERN apresentaram um incremento relativo de 22,19% na eficiência de conversão de potência, ao passo que aqueles com NPs TMN exibiram uma melhoria de 13,23%. Tais ganhos são atribuídos primordialmente à eficiente emissão por conversão descendente do íon Eu^{3+} e à superior passivação superficial conferida pela arquitetura caroço-casca. Em conjunto, esses mecanismos suprimem as perdas por recombinação e otimizam a dinâmica dos portadores de carga. Estes resultados evidenciam o potencial de materiais fotoconversores à base de lantanídeos para superar as limitações inerentes à absorção espectral das CSPs, apresentando-se como uma estratégia promissora para o desenvolvimento de tecnologias fotovoltaicas de próxima geração.

Palavras-chave: conversão espectral; nanopartículas; lantanídeos; células solares de perovskita

LIST OF FIGURES

LIST OF TABLES

LIST OF SYMBOLS

$I(t)$	Photoluminescence intensity at time t
I_0	Background intensity
V_{OC}	Open-circuit voltage
τ	Emission lifetime
J_{SC}	Short-circuit current density
Ag	Silver
CF_3COOH	Trifluoroacetic acid
$C_2H_6O_2$	Ethylene glycol
Er_2O_3	Erbium oxide
Er^{3+}	Erbium ion
$EuCl_3$	Europium chloride
Eu^{3+}	Europium ion
Gd_2O_3	Gadolinium oxide
$GdCl_3$	Gadolinium chloride
$Ln(TFA)_3$	Lanthanide trifluoroacetate
Ln^{3+}	Lanthanide ion
MAI	Methylammonium iodide
$MAPbI_3$	Methylammonium lead iodide (perovskite)
Na(TFA)	Sodium trifluoroacetate
$NaGdF_4$	Sodium gadolinium fluoride
$NaGdF_4:Yb^{3+},Er^{3+}@NaGdF_4:Eu^{3+}$	Sodium gadolinium fluoride nanoparticle doped with ytterbium, erbium, and europium (ERN)

$NaGdF_4:Yb^{3+},Tm^{3+}@NaGdF_4:Eu^{3+}$	Sodium gadolinium fluoride nanoparticle doped with ytterbium, thulium, and europium (TMN)
$NaOH$	Sodium hydroxide
NH_4F	Ammonium fluoride
NiO_x	Nickel oxide
OA	Oleic acid
ODE	1-Octadecene
OM	Oleylamine
PCBM	Phenyl-C61-butyric acid methyl ester
Yb^{3+}	Ytterbium ion
α-$NaGdF_4$	Alpha-phase sodium gadolinium fluoride
β-$NaGdF_4$	Beta-phase sodium gadolinium fluoride

LIST OF ABBREVIATIONS AND ACRONYMS

BCP	Bathocuproine
CET	Cooperative Energy Transfer
DC	Downconversion
DFT	Density Functional Theory
DLS	Dynamic Light Scattering
DMF	Dimethylformamide
DMSO	Dimethyl sulfoxide
DS	Downshifting
EQE	External Quantum Efficiency
ERN	$NaGdF_4:Yb^{3+},Er^{3+}@NaGdF_4:Eu^{3+}$
ESA	Excited-State Absorption
ETL	Electron Transport Layer
ETU	Energy Transfer Upconversion
FF	Fill Factor
FTIR	Fourier-Transform Infrared Spectroscopy
HOMO	Highest occupied molecular orbital
HTL	Hole Transport Layer
ITO	Indium tin oxide
LUMO	Lowest unoccupied molecular orbital
NP	Nanoparticle
PA	Photon Avalanche
PCE	Power Conversion Efficiency

PCBM	Phenyl-C61-butyric acid methyl ester
PL	Photoluminescence
PLQY	Photoluminescence Quantum Yield
PSC	Perovskite Solar Cell
PV	Photovoltaic
QY	Quantum Yield
SAED	Selected Area Electron Diffraction
TEM	Transmission Electron Microscopy
TMN	$NaGdF_4:Yb^{3+},Tm^{3+}@NaGdF_4:Eu^{3+}$
UC	Upconversion
UV	Ultraviolet
UV-Vis	Ultraviolet–Visible Spectroscopy
XRD	X-ray Diffraction

CONTENTS

1 INTRODUCTION AND OBJECTIVES

1.1 Introduction

The increasing global demand for energy, coupled with the urgent need to reduce greenhouse gas emissions and mitigate climate change, has accelerated the transition to clean, sustainable energy sources. Among these alternatives, photovoltaic (PV) technologies, which directly convert sunlight into electricity, have emerged as a promising solution to address contemporary energy challenges. The Earth continuously receives about 173,000 TW of solar power on its surface (land and oceans) (1), which far exceeds the world's annual electricity consumption. According to the International Energy Agency (IEA), global electricity generation in 2024 reached approximately 1,080.1 TWh, reflecting continued growth in energy demand (2).

Perovskite solar cells (PSCs) have gained significant attention as one of the most innovative PV technologies, offering high power conversion efficiency (PCE), with a record of 28.4% (3). Beyond efficiency, PSCs combine cost-effective fabrication, compatibility with flexible substrates and portable devices, and excellent performance under low-light conditions, such as cloudy weather. These advantages make PSCs a strong candidate to expand the global solar energy market, paving the way for affordable and sustainable electricity supply (4, 5).

Despite rapid progress, PSCs face critical challenges, particularly their limited long-term stability due to photo-induced degradation and their restricted absorption range, which prevents efficient harvesting of sub-bandgap photons. These limitations lead to energy losses and hinder the full performance potential of PSCs (6). Addressing these issues, improving spectral absorption, mitigating degradation, and enhancing stability, is essential for advancing PSC technology toward large-scale deployment (7, 8).

A promising strategy is to incorporate lanthanide-doped nanoparticles (NPs) into PSCs. Due to their unique electronic structure, characterized by partially filled $4f$ orbitals, lanthanides can convert photons from the near-infrared and ultraviolet regions into visible light (9, 10). Their luminescence arises from intra-$4f$ transitions, which, although parity-forbidden, enable photon-conversion processes such as upconversion, downconversion, and downshifting. These processes typically exhibit sharp emission lines and long lifetimes (microseconds to milliseconds), enhancing photon management and the optical performance of PSCs.

In this work, we investigate the incorporation of two core–shell nanoparticle systems, $NaGdF_4$:Yb^{3+},Tm^{3+}@$NaGdF_4$:Eu^{3+} (TMN) and $NaGdF_4$:Yb^{3+},Er^{3+}@$NaGdF_4$:Eu^{3+} (ERN), as

interfacial layers in PSCs. These nanostructures exhibit dual photon-conversion capabilities: upconversion (via Yb^{3+}/Tm^{3+} or Yb^{3+}/Er^{3+} in the core) and downshifting (via Eu^{3+} in the shell), effectively extending the spectral response of the device. The spatially selective doping of distinct lanthanide ions into the core and the shell is uncommon and represents a key innovation of this work. The nanoparticles were synthesized via a high-temperature, high-pressure thermal decomposition route, ensuring high crystallinity and phase purity. They were incorporated into PSCs without ligand removal, highlighting the dominant role of their optical effects.

While the focus of this study is PSC applications, $NaGdF_4$ nanoparticles are versatile, with uses in bioimaging, diagnostics, drug delivery, and photodynamic therapy (11–13), as well as sensing and anticounterfeiting (14, 15). Importantly, toxicity tests were performed on $NaGdF_4$ nanoparticles synthesized via a solvothermal route, which differs from the decomposition route used for PSC-optimized nanoparticles, and are presented in Appendix A, supporting their safe use.

1.2 Objectives

The primary objective of this work is to synthesize and characterize core and core-shell nanoparticles doped with rare-earth ions that exhibit upconversion and downshifting properties, with the aim of enhancing the power conversion efficiency of perovskite solar cells. Specifically, the objectives are to:

(a) Synthesize core nanoparticles $NaGdF_4$:Yb^{3+},Er^{3+} and $NaGdF_4$:Yb^{3+},Tm^{3+} with upconversion properties;

(b) Synthesize core-shell nanoparticles with a $NaGdF_4$:Eu^{3+} shell, exhibiting downshifting properties;

(c) Characterize the structural, morphological, optical, and photophysical properties of the synthesized nanoparticles and correlate them with photovoltaic performance;

(d) Fabricate perovskite solar cells with and without nanoparticles;

(e) Evaluate the photovoltaic performance of the devices using solar simulator measurements and external quantum efficiency (EQE) analysis to assess the impact of the nanoparticles.

2 STATE-OF-THE-ART REVIEW

2.1 Lanthanides

Lanthanides (Ln) are elements of the sixth period of the periodic table, with atomic numbers ranging from 58 (cerium) to 71 (lutetium), characterized by the occupation of the $4f$ orbitals. The most common oxidation state is +3, while the +2 and +4 states are less stable and readily revert to +3 (16).

The optical properties of lanthanides originate from the $f - f$ electronic transitions of Ln^{3+} ions. These $4f$ electrons are shielded by the $5s^2$ and $5p^6$ levels, rendering their transitions relatively insensitive to the chemical environment (17). Consequently, the spectra exhibit sharp, well-defined lines at specific wavelengths. According to the Laporte rule, these transitions are forbidden, resulting in long lifetimes, typically in the μs to ms range (18).

In nanoparticles, the degenerate $(2J + 1)$ levels of Ln^{3+} ions are perturbed by the ligand or crystal field, slightly shifting emission wavelengths, altering transition intensities, and affecting excited-state lifetimes (19)

2.2 Luminescent Materials and Host Matrices

Luminescent materials emit light upon excitation by an external energy source (20). Typically, these materials consist of inorganic solids, referred to as host matrices, doped with Ln^{3+} ions as active centers. Energy absorption can occur through both the host lattice and the dopant ions, with energy transfer via the lattice. Light emission primarily originates from the intentionally doped rare-earth ions, which are present at low concentrations (a few mol% or less) (21). Figure 1 illustrates the energy transfer mechanisms and the main luminescent transitions of Ln^{3+} ions.

The crystal structure of the host strongly influences the optical properties, making careful selection of the host matrix essential to optimize upconversion, downconversion, and downshifting efficiency. Hosts such as $NaYF_4$ (23–29) and $NaGdF_4$ (30–32) are frequently chosen due to their favorable optical properties, high quantum efficiency, and good stability, enabling efficient generation of higher- or lower-energy photons.

$NaLnF_4$ nanoparticles can adopt two crystal phases: cubic (α) and hexagonal (β). The β-phase is recognized as more efficient due to its unique crystal structure, making it the

Figure 1 – a) Partial 4*f*-energy level diagram for trivalent lanthanide activators. b) Main luminescent transitions of the lanthanide activators in the electromagnetic spectrum.

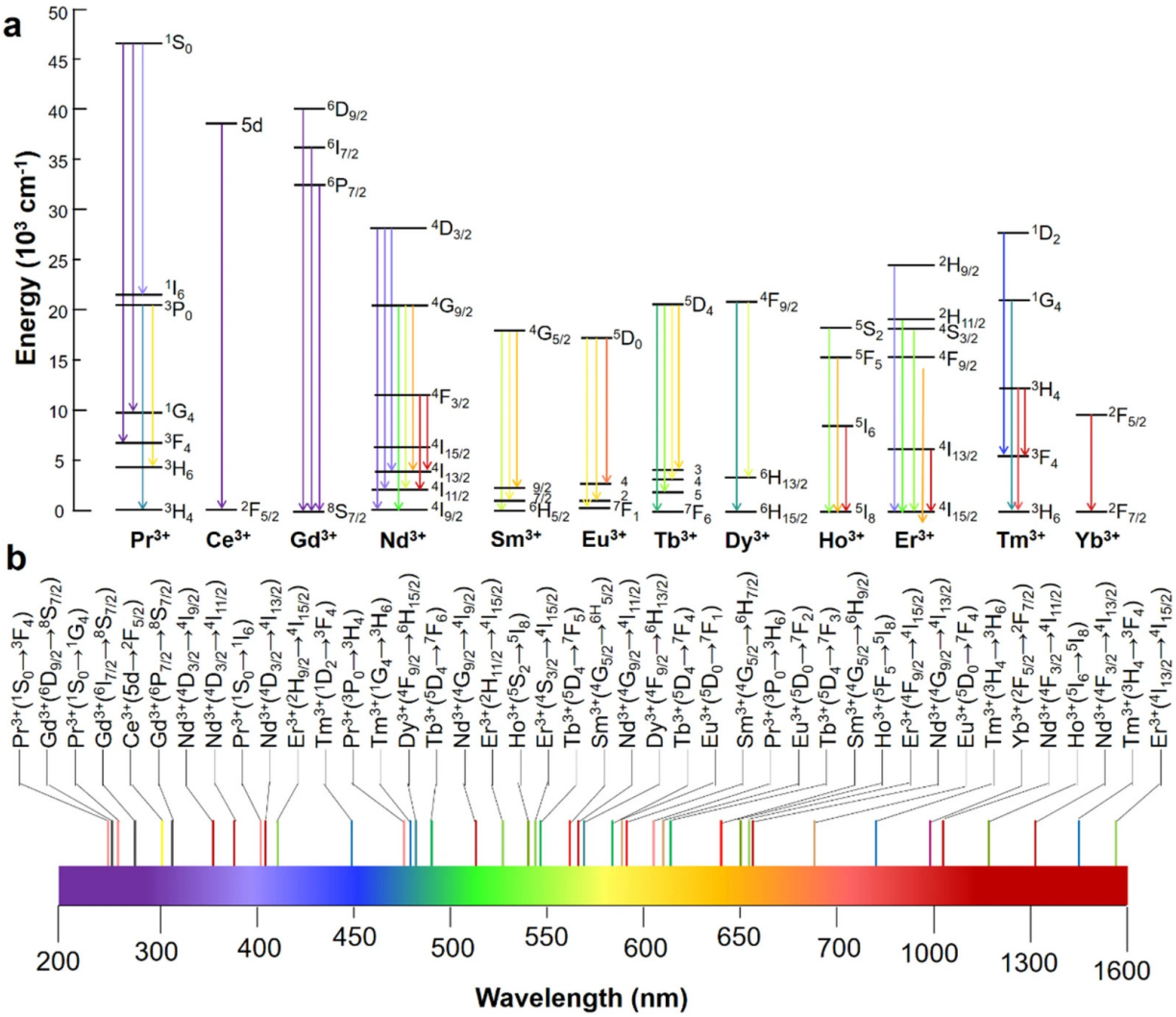

Source: Lei *et al.*, 2022 (22).

preferred host lattice at the nanoscale for decades (33, 34). Figure 2 presents a schematic overview of the general strategy used to achieve dual-mode Eu^{3+} luminescence in $NaGdF_4$, highlighting how the structural design enables both upconversion and downshifting processes.

To enhance emission efficiency, the use of core–shell architectures has become a widely adopted approach (12, 35, 36). In these systems, the core contains the optically active ions (such as Eu^{3+}), while the shell, typically undoped or doped with sensitizers, serves to passivate surface defects, reduce non-radiative losses, and improve energy transfer pathways. This structural configuration effectively isolates the luminescent centers from surface quenching and enhances both high and low energy photon conversion, resulting in stronger and more stable dual-mode luminescence.

Figure 2 – Schematic illustration of the general strategy to achieve the dual-mode luminescence of Eu^{3+} in $NaGdF_4$.

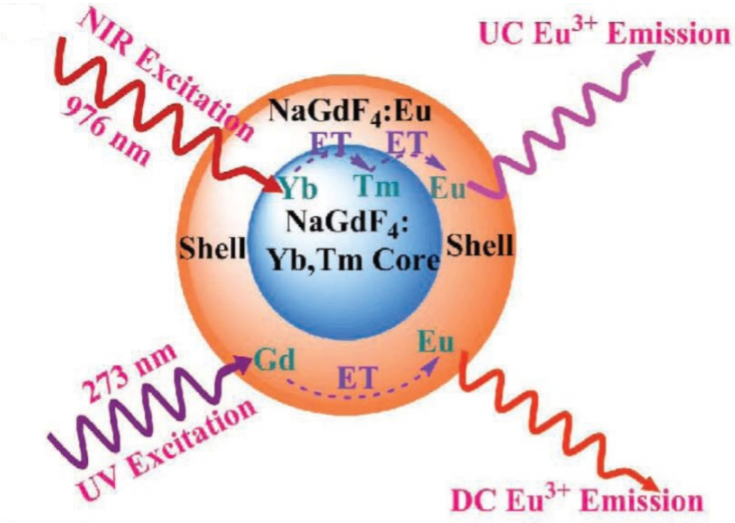

Source: Liu *et al.*, 2010 (37).

2.3 Emission Mechanisms

Depending on the lanthanide ion doped into the host matrix, different types of luminescence can occur. The three typical energy transfer mechanisms of Ln^{3+} ions are downshifting (DS), downconversion (DC), also known as quantum cutting (QC), and upconversion (UC), illustrated in Figure 3b. In addition, some representative excited energy levels involved in UC for trivalent lanthanides are shown in Figure 3a.

Downshifting refers to the absorption of a high-energy photon (typically UV or visible) followed by the emission of a lower-energy photon (generally in the visible range) (33, 38).

Downconversion occurs when a high-energy photon (UV or visible) is converted into two or more lower-energy photons (in the visible range) (39–41).

Upconversion is a nonlinear anti-Stokes optical process in which two or more low-energy photons (near-infrared) are converted into a single higher-energy photon (visible) (39, 42, 43). It was first observed in 1966 by François Auzel, involving energy transfer between sensitizer and activator ions (44).

2.4 Luminescence Mechanisms

Figure 4 illustrates the main photon conversion mechanisms in lanthanide-doped luminescent materials. In Figure 4a, the downshifting process is shown, where a high-energy

Figure 3 – Schematic illustration of the three energy transfer mechanisms of Ln^{3+}. From left to right: downshifting, downconversion, and upconversion. Solid upward and downward arrows represent photon excitation and emission processes, respectively, while the dashed line indicates non-radiative relaxation.

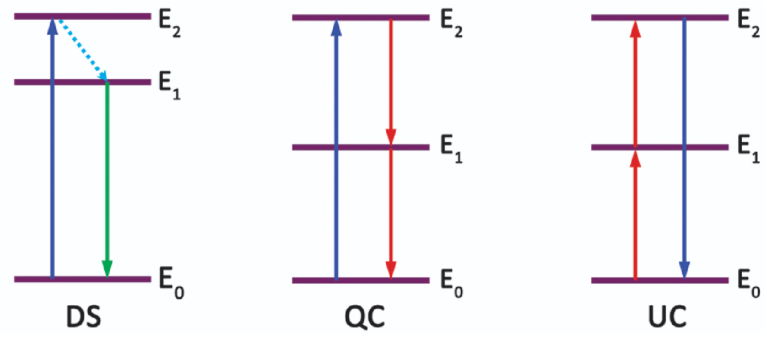

Source: Dong *et al.*, 2015 (33).

photon is absorbed and re-emitted as a single lower-energy photon. Figure 4b depicts the downconversion or quantum cutting process, in which one high-energy photon is converted into two lower-energy photons. Finally, Figure 4c presents the different upconversion mechanisms, in which two or more low-energy photons are absorbed, leading to the emission of a higher-energy photon. In this case, distinct excitation pathways are represented, namely excited-state absorption (ESA), energy transfer upconversion (ETU), photon avalanche (PA), cooperative energy transfer (CET), and energy migration upconversion (EMU).

2.4.1 Downshifting and Downconversion

1. **Downshifting:** A lanthanide ion absorbs a high-energy (short-wavelength) photon and subsequently emits a single photon of lower energy (longer wavelength) (46) (see Figure 4a).
2. **Downconversion or Quantum Cutting:** In this process, a single high-energy photon is converted into two or more lower-energy photons, leading to a potential photoluminescence quantum yield (PLQY) above 100% (47). Two main QC mechanisms are proposed: (i) sequential photon emission from a single lanthanide ion (photon cascade effect), where a three-level system enables two-step emission of NIR photons (48, 49), and (ii) cooperative interactions between two luminescent centers, where the absorbed energy is shared to produce two NIR photons through energy transfer (see Figure 4b).

Figure 4 – a) Schematic diagram of the downshift luminescence process in Ln-doped materials. b) Schematic representation of downconversion (DC) or quantum cutting (QC) luminescence mechanisms. c) Schematic representation of upconversion (UC) processes: ESA = excited-state absorption, ETU = energy transfer upconversion, PA = photon avalanche, CET = cooperative energy transfer, and EMU = energy migration upconversion. In the diagram, ① denotes nonradiative relaxation processes, and ② represents energy transfer processes.

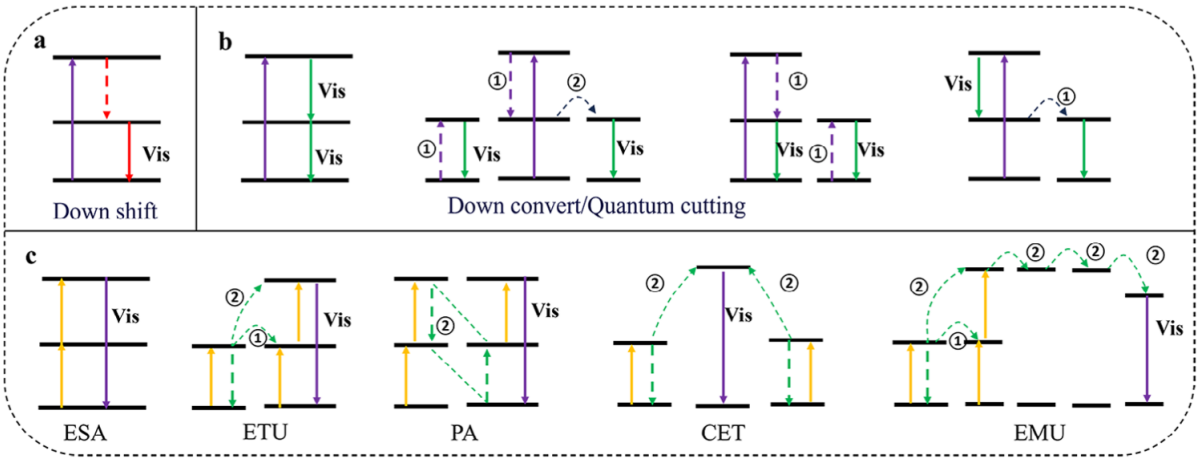

Source: Wang *et al.*, 2025 (45).

2.4.2 Upconversion

In contrast to DS and DC, upconversion involves the absorption of two or more low-energy photons followed by the emission of a higher-energy photon. The main UC mechanisms are (see Figure 4c):

1. **Excited-state absorption (ESA):** A single ion sequentially absorbs two or more photons, being promoted stepwise to higher excited states. After nonradiative relaxation, the ion emits an upconverted photon. This process does not rely on ion–ion interactions, and thus works efficiently at low doping levels (50).
2. **Energy transfer upconversion (ETU):** Two neighboring ions are involved, typically a sensitizer and an activator. Both are excited to intermediate states, after which the sensitizer transfers its energy nonradiatively to the activator, promoting it to a higher excited state. ETU is usually more efficient than ESA due to the larger absorption cross-section of sensitizers (33).
3. **Photon avalanche (PA):** Initiated by weak ground-state absorption followed by ESA, this

process is reinforced by a feedback loop of cross-relaxation events between excited and ground-state ions. The result is an avalanche-like increase in excited-state population and upconversion emission (51).

4. **Cooperative energy transfer (CET):** Involves a three-ion interaction, where two sensitizer ions simultaneously transfer their energy to an activator ion, promoting it to a higher excited state. The probability of this cooperative process is generally low (52).
5. **Energy migration upconversion (EMU):** Specific to core–shell nanostructures, this process involves four types of ions: sensitizer, accumulator, migrator, and activator. The sensitizer absorbs incident photons and transfers the energy to the accumulator, which then passes it to the migrators. The energy migrates through the host lattice until it reaches an activator, which emits the upconverted photon (53).

2.5 Perovskite Solar Cells

Perovskite solar cells (PSCs) exhibit remarkable power conversion efficiencies, making them an up-and-coming technology for photovoltaic energy. However, their commercialization is hindered by stability issues arising from moisture, oxygen, light, temperature, and electrical bias. Strategies such as material engineering, defect passivation, interface optimization, and advanced encapsulation have shown potential to enhance stability, while advanced characterization techniques provide insights into degradation pathways. Despite significant progress in efficiency, achieving long-term operational stability remains challenging. Future research should focus on developing structurally robust perovskites, improving encapsulation methods, gaining a molecular-level understanding of degradation mechanisms, and accelerating testing to ensure durable performance. Addressing these challenges will enable PSCs to become major contributors to renewable energy generation (54).

The architecture illustrated in Figure 5a corresponds to an inverted (p–i–n) PSC configuration. The structure begins with a transparent, conductive ITO (indium tin oxide) substrate that allows light to enter and serves as an electrode. A NiO_x layer is deposited on top, functioning as a hole transport layer (HTL) to facilitate the selective extraction of positive carriers. The active perovskite layer, for example, methylammonium lead iodide ($MAPbI_3$), absorbs incident photons and generates electron–hole pairs. Above it, the PCBM layer (phenyl-C_{61}-butyric acid methyl ester) acts as an electron transport layer (ETL), selectively conducting photogenerated electrons. To improve energy alignment and block unwanted holes, an ultrathin

BCP (bathocuproine) layer is inserted. Finally, electron extraction is completed via the metallic Ag electrode, closing the external circuit (55, 56).

Figure 5 – Schematic diagrams of (A) the device structure of ITO/NiO_x/ Perovskite/PCBM/BCP/Ag; and (B) the corresponding energy band diagrams for the inverted perovskite solar cell.

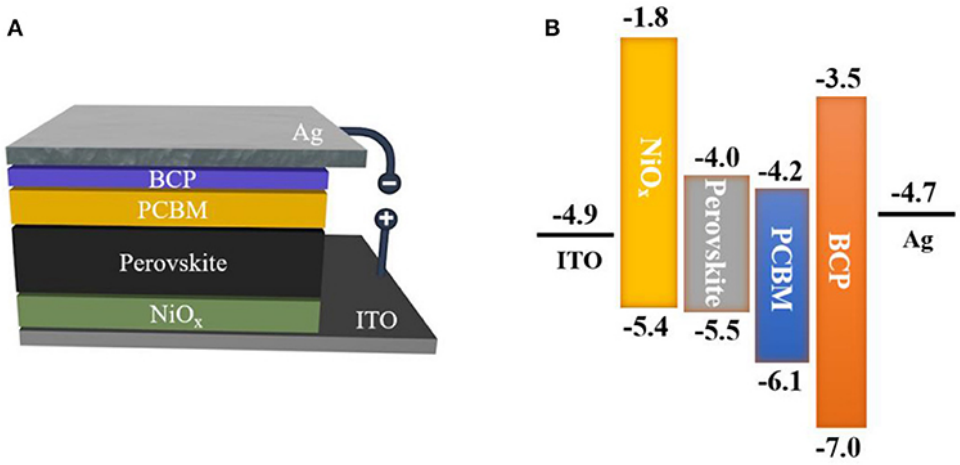

Source: He *et al.*, 2018 (57).

The energy conversion process occurs as follows: when light illuminates the perovskite layer ($MAPbI_3$), photons with energy above the band gap (1.60 eV) excite electrons from the valence band (−5.5 eV) to the conduction band (−4.0 eV), forming electron–hole pairs. The band alignment shown in Figure 5b ensures selective carrier transport: the conduction band of PCBM (−4.2 eV) lies slightly below that of the perovskite, providing a favorable driving force for electrons to flow from the perovskite into the ETL, while its deeper lowest unoccupied molecular orbital (LUMO, −6.1 eV) prevents hole leakage. On the opposite side, the valence band of NiO_x (−5.4 eV) is well aligned with the perovskite valence band, enabling efficient hole transfer while its high conduction band edge (−1.8 eV) blocks electron backflow. The thin BCP layer, with a deep highest occupied molecular orbital (HOMO) of −7.0 eV and a LUMO of around −3.5 eV, further prevents hole injection into the Ag cathode while still permitting electron transport. The Ag electrode, with a Fermi level near −4.7 eV, efficiently collects electrons from PCBM (58–60).

Thus, the well-aligned energy levels of each layer enable selective charge transport and carrier extraction while suppressing interfacial recombination. This energetic arrangement is fundamental to achieving high photocurrent and overall performance in inverted PSCs.

2.6 Enhancing Perovskite Solar Cells with Lanthanide-Based Nanoparticles

The theoretical efficiency limit of a single-junction solar cell, established by Shockley and Queisser, is approximately 30% (61), assuming an ideal semiconductor absorber under AM 1.5 illumination with unity external quantum efficiency. In practice, PSCs experience losses due to carrier recombination (62, 63), incomplete absorption and reflection (64), and parasitic resistances (65).

A significant challenge is the spectral mismatch between the solar spectrum and the perovskite absorption range: sub-bandgap photons are not absorbed, while high-energy photons rapidly thermalize, dissipating excess energy as heat. Spectral management via downconversion, downshifting, and upconversion processes mitigates these losses (66), converting sub-bandgap NIR photons into visible light or splitting high-energy UV photons into lower-energy photons. By expanding the usable spectral range, such strategies improve electron–hole pair generation and overall efficiency, as illustrated in Figure 6.

Figure 6 – Spectral irradiance of the solar spectrum and energy conversion mechanisms relevant to PSCs. The orange region indicates the absorption range of perovskite cells. DC processes convert high-energy photons into lower-energy photons, while UC processes combine low-energy photons to generate higher-energy photons. Colored arrows represent typical photon transitions involved in these processes.

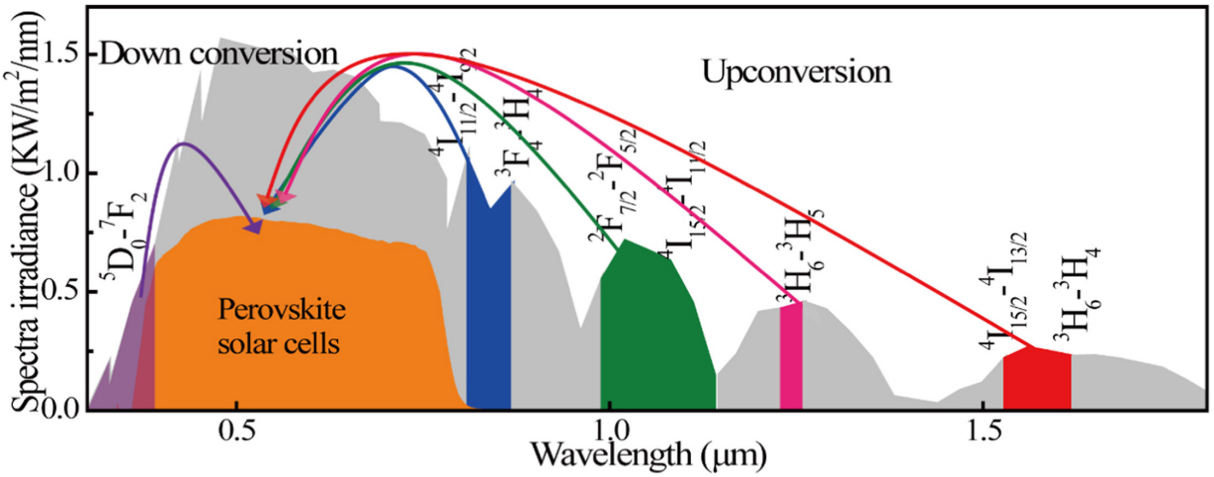

Source: Li *et al.*, 2018 (67).

Beyond efficiency, UC and DC layers can also enhance long-term stability and photostability by serving as protective encapsulation layers. Several strategies have been reported

for integrating lanthanide-based nanoparticles (NPs) into PSCs, employing upconversion, down-conversion, and hybrid nanostructures. These approaches have led to consistent improvements in power conversion efficiency (PCE), with the magnitude of enhancement depending on the NP composition and device configuration.

Table 1 summarizes representative studies, highlighting pristine device efficiencies, PCE values after NP incorporation, and the relative performance gains.

Table 1 – Reported improvements in PSCs using lanthanide-based nanoparticles.

Nanoparticles	**Method**	**PCE (%)**	**PCE-NP (%)**	**Gain (%)**	**Ref.**
$NaYF_4$:Yb,Er,Er/$NaYF_4$:Yb,Er,Tm/Ag + $Eu(TTA)_2(Phen)MAA$	cold pressing	16.10	19.50	21.10	(67)
β-$NaYF_4$:Yb,Er	thermolysis	12.05	18.60	19.70	(68)
KYF_7F_{22}:20%Yb/5%Er	co-precipitation	11.50	12.25	06.50	(69)
β-$NaGdF_4$:Yb,Er	solvothermal	18.01	21.10	17.16	(70)
β-$NaYF_4$:Yb,Er@SiO_2	hydrothermal	08.19	09.92	21.12	(71)
$NaGdF_4$:Yb,Er@$NaGdF_4$:Eu	hydrothermal	12.85	14.21	10.58	(35)
$LiYF_4$:Yb,Er + CQDs	hydrothermal	16.65	18.15	09.01	(72)
$YLiF_4$:Yb,Er	thermolysis	19.45	21.32	10.13	(73)
$NaCsWO_3$@$NaYF_4$@$NaYF_4$:Yb,Er	solvothermal	16.01	18.89	17.99	(74)
β-$NaYF_4$:Yb,Tm@TiO_2	solvothermal	13.98	16.27	16.38	(36)

Source: Author.

The percentage gain (Gain (%)) shown in Table 1 was calculated based on the relative variation between the PCE of the pristine perovskite solar cell and that obtained after nanoparticle incorporation (PCE-NP). The calculation follows the expression:

$$\text{Gain (\%)} = \frac{(\text{PCE-NP} - \text{PCE})}{\text{PCE}} \times 100 \tag{2.1}$$

This value represents the relative increase in photovoltaic efficiency provided by the incorporation of lanthanide-based nanoparticles, allowing the quantification of their positive impact on PSC performance.

3 MATERIALS AND METHODS

3.1 Materials

The materials used in the synthesis and fabrication processes included gadolinium oxide (Gd_2O_3, 99.9%), ytterbium oxide (Yb_2O_3, 99.9%), thulium oxide (Tm_2O_3, 99.9%), and erbium oxide (Er_2O_3, 99.9%) as lanthanide sources for the preparation of lanthanide trifluoroacetates ($Ln(TFA)_3$), all supplied by Sigma-Aldrich (Merck KGaA). Trifluoroacetic acid (CF_3COOH, ≥99.0%), sodium hydroxide (NaOH, ≥97.0%), octadecene (ODE, 90.0%), oleic acid (OA, 90.0%), oleylamine (OM, 70%), ethanol (≥95.0%), cyclohexane (≥99.0%), distilled water, and toluene (≥99.9%) were also used. Indium tin oxide (ITO)-coated glass substrates (XY15S, 15 Ω/sq) from Xinyan Technology Ltd and 99.99% purity nickel oxide (NiO_x) sputtering targets from Super Conductor Materials, Inc., were used for PSC fabrication. Methylammonium iodide (MAI, ≥99.9%), lead iodide (PbI_2, ≥99.999%), dimethylformamide (DMF, ≥99.8%), dimethyl sulfoxide (DMSO, ≥99.9%), bathocuproine (BCP, ≥99.99%), and chlorobenzene (≥99.0%) were supplied by Sigma-Aldrich (Merck KGaA). Phenyl-C61-butyric acid methyl ester (PCBM, ≥99.0%) was obtained from Ossila, and silver (Ag) was used for back contact deposition.

3.2 Methods

3.2.1 Nanoparticle synthesis

The synthesis of nanoparticles (NPs) with upconversion and downshifting properties was performed using the high-temperature decomposition method in high-boiling-point solvents, hereafter referred to as thermolysis. In this method, salts containing lanthanide ions (Ln^{3+}) are decomposed in solvent mixtures with high boiling points, typically around 300 °C, such as octadecene, oleic acid, and oleylamine (75). The formation, crystal structure, morphology, chemical composition, and optical properties of sodium/yttrium-gadolinium tetrafluoride NPs strongly depend on the precursors used, temperature, and reaction time.

The NPs used in this work were obtained following methods adapted from the literature (24, 76) and further optimized by Rodrigues *et al.* (77, 78) and Calado *et al.* (25). The schematic of the NPs preparation is shown in Figure 7.

Initially, lanthanide trifluoroacetates ($Ln(TFA)_3$) were prepared by dissolving 1.0 g of Ln_2O_3 in 32 mL of a 1:1 mixture of distilled water and trifluoroacetic acid under reflux at 70 °C

Figure 7 – Schematic illustration of the thermolysis synthesis of β-$NaGdF_4$:Yb,Er@$NaGdF_4$ core–shell nanoparticles.

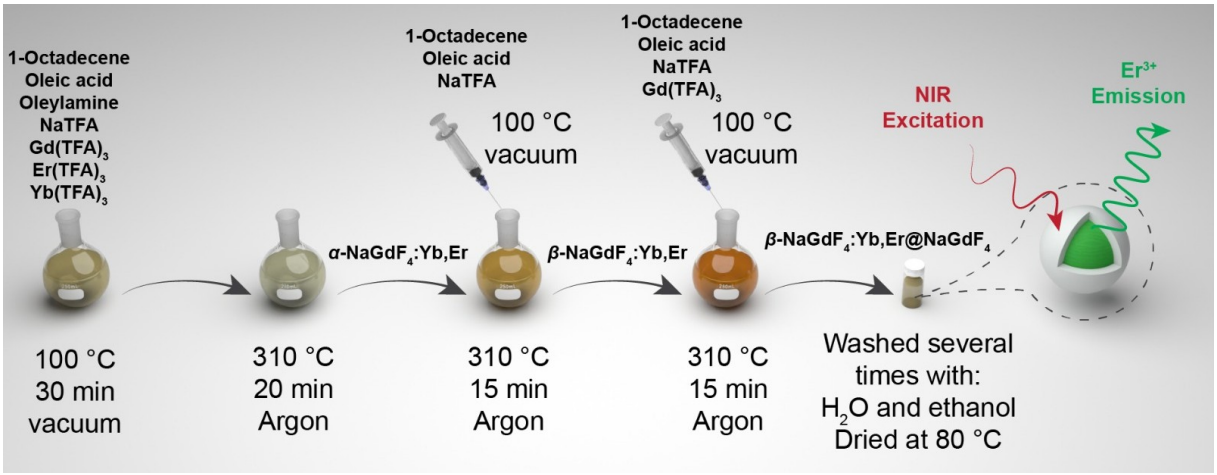

Source: Maturi (2025, unpublished).

until a clear solution was obtained. Excess water and acid were removed by continuous heating and stirring, yielding $Ln(TFA)_3$. Sodium trifluoroacetate, Na(TFA), was prepared similarly from NaOH.

For the synthesis of the β-$NaGdF_4$ host matrix, $Gd(TFA)_3$ and Na(TFA) were mixed in a flask with octadecene, oleic acid, and oleylamine, heated at 100 °C under vacuum for 30 min, producing a yellowish solution. The temperature was then raised to 310 °C under an Ar atmosphere for 20 min, during which α-$NaGdF_4$ formed. Simultaneously, an excess solution of sodium and fluoride was prepared and rapidly added to the system after α-$NaGdF_4$ formation, followed by heating to 330 °C for 15 min. The system was cooled under Ar and allowed to rest overnight.

The NPs were precipitated with ethanol, centrifuged, and repeatedly washed with cyclohexane and ethanol to remove excess organic compounds, then washed with water and ethanol, and finally dried at 80 °C.

Core nanoparticles, β-$NaGdF_4$:Yb^{3+},Tm^{3+} and β-$NaGdF_4$:Yb^{3+},Er^{3+}, were synthesized using stoichiometric amounts of $Ln(TFA)_3$: 1.2 mmol $Gd(TFA)_3$, 0.27 mmol $Yb(TFA)_3$, 1.5 mmol Na(TFA)0.03 mmol, and $Tm(TFA)_3$ or $Er(TFA)_3$. For core–shell NPs, after the core formation step, the reaction temperature was reduced to 260 °C, and the shell precursors were added in two injections, following the same heating and cooling protocol. For core–shell NPs with Eu^{3+} doping, the injections contained 0.35 mmol $Gd(TFA)_3$, 0.15 mmol $Eu(TFA)_3$, and 0.5 mmol Na(TFA).

3.2.2 Device fabrication

The devices were fabricated using a glass/ITO/NiO_x/NPs/Perovskite/PCBM/BCP/Ag architecture, widely reported in the literature (79–81). In this configuration, ITO serves as a transparent, conductive electrode, while NiO_x acts as a stable, efficient hole-transport layer (HTL). The $MAPbI_3$ perovskite serves as the active layer, generating charge carriers upon illumination. PCBM is used as the electron transport layer (ETL), and BCP prevents interfacial recombination before electron collection at the Ag top electrode. This arrangement ensures efficient charge extraction and overall device performance.

NiO_x films (40 nm) were deposited by RF magnetron sputtering at 150 W under an argon atmosphere of 4×10^{-3} mbar. All precursor solutions were prepared and handled in a nitrogen-filled glovebox.

The $MAPbI_3$ precursor was obtained by dissolving equimolar MAI and PbI_2 in a 9:1 (v/v) DMF:DMSO mixture to form a 1.2 M solution, stirred at 60 °C for 4 h and equilibrated overnight. The solution was filtered through a 0.22 μm PTFE syringe filter. PCBM (20 mg/mL in chlorobenzene) and BCP (1 mg/mL in ethanol) solutions were prepared separately.

Perovskite and ETL layers were deposited by spin-coating. $MAPbI_3$ films were formed using a two-step program (2,000 rpm for 10 s, then 4,000 rpm for 20 s), with chlorobenzene dropped after 3 s at maximum speed, followed by annealing at 125 °C for 10 min. PCBM was deposited dynamically (60 μL; 1,500 rpm for 15 s, then 2,000 rpm for 20 s) and dried at 70 °C for 1 min. BCP was spin-coated at 4,000 rpm for 40 s. Silver top electrodes (150 nm, 0.10 cm^2) were deposited by thermal evaporation.

For PSCs incorporating nanoparticles, an NP layer was added on top of the NiOx HTL. A dispersion of 1 mg of NPs in 1 mL of toluene was spin-coated (250 μL, 2,000 rpm for 30 s) and annealed at 40 °C for 1 min. Each device comprised an array of 10 individual solar cells. Figure 8 provides an overview of the device configuration and measurement setup: panel (a) shows the electrical characterization system used for current–voltage measurements under simulated illumination; panel (b) presents a schematic of the multilayer architecture (glass/ITO/NiOx/NPs/Perovskite/PCBM/BCP/Ag) highlighting the position of the NP layer within the stack; and panel (c) displays a photograph of the fabricated substrate containing the 10 PSCs, each with an active area of 2 mm × 5 mm used for performance evaluation.

Figure 8 – (a) Photograph of the electrical characterization setup used for current–voltage measurements of the PSCs. (b) Schematic representation of the glass/ITO/NiO_x/NPs/Perovskite/PCBM/BCP/Ag device architecture. (c) Image of a fabricated device showing the individual cell areas (2 mm × 5 mm).

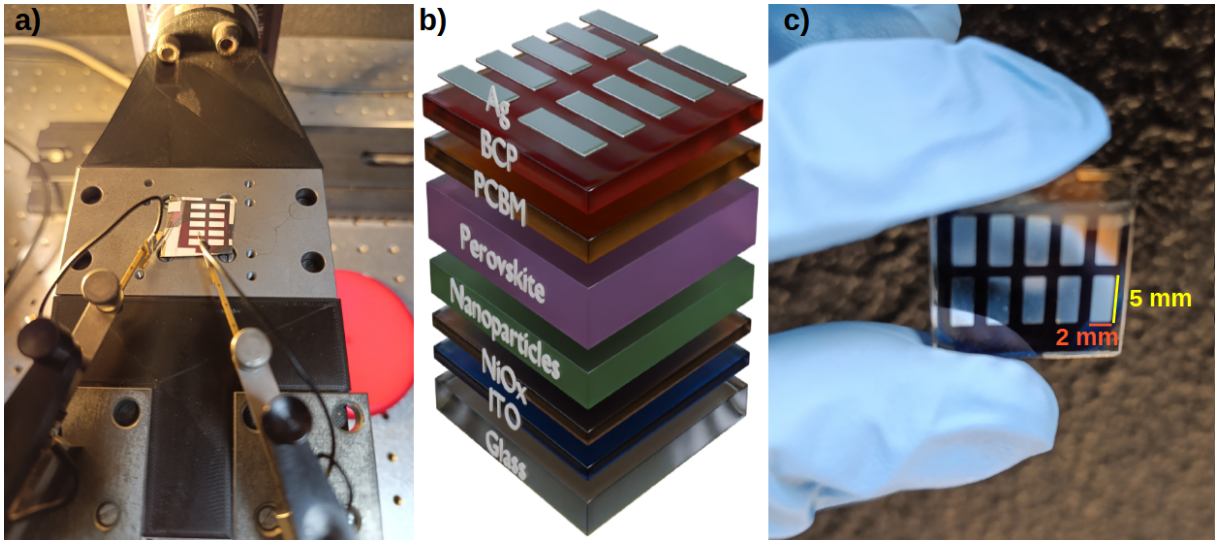

Source: a) and c) Author, 2025. b) Maturi (2025, unpublished).

3.2.3 Characterization techniques

X-ray diffraction (XRD) measurements were conducted using a Shimadzu XRD-6000 diffractometer, operated at 40 kV and 30 mA with CuKα radiation. Diffraction patterns were recorded in the angular range of 10° to 65°, with a step size of 0.02° and a scan speed of 2°/min. Slits of 1° were used for divergence and scattering, while a 0.30 mm slit was employed for reception.

A JEOL JEM-2100 was utilized for transmission electron microscopy (TEM) imaging, selected area electron diffraction (SAED), and energy dispersive X-ray spectroscopy (EDS). The system operates with a LaB_6 electron source at 200 kV, achieving spatial resolutions of 0.25 nm in TEM mode and 0.2 nm in scanning transmission electron microscopy (STEM) mode. EDS mapping was performed to analyze the elemental distribution, while high-resolution bright-field STEM imaging and CMOS cameras (4k×4k) captured detailed images and electron diffraction patterns of nanometric regions.

Emission and excitation spectra of the nanoparticle samples were measured using a FluoTime 300 spectrofluorometer (FT300, PicoQuant) with an additive emission monochromator featuring a grating with 1200 grooves mm^{-1} blazed at 500 nm (reciprocal linear dispersion of 1.4

nm mm^{-1}). The system was coupled to a photomultiplier (PMA-C 192-N-M, PicoQuant) and operated in right-angle acquisition mode, with a 300-W Xenon arc lamp as the excitation source. Spectra were recorded at room temperature (298 K) with an integration time of 0.5 s and a spectral resolution of 0.5 nm. The emission spectra were corrected for the spectrofluorometer's detection and optical spectral response, while the excitation spectra were corrected for the lamp's spectral intensity distribution using a photodiode reference detector. Upconverting emission spectra were measured using a 980 nm laser diode (LDH-P-C-980MB, PicoQuant) as the excitation source, operating at a power density of 62 W cm^{-2}. Intensity decay profiles were recorded using the same equipment, with a 10 W Xe flash lamp and the 980 nm laser in pulsed mode as excitation sources, and monitoring Eu^{3+} emission at 615 nm. The decay curves were adjusted to a mono-exponential decay function $I(t) = I_0 + A \cdot e^{-\frac{t}{\tau}}$, where $I(t)$ is the photoluminescence intensity at the time t, I_0 is the background intensity, τ is the emission lifetime, and A is the amplitude.

Quantum yield (QY) measurements were performed using a Hamamatsu C13534 system equipped with a 150 W xenon lamp as the excitation source. This system enables precise determination of absolute quantum yield by integrating the emitted light over all angles, thereby eliminating the need for comparative standards. The setup includes an integrating sphere coated with a highly reflective material to ensure accurate light collection, as well as a spectrometer for analyzing excitation and emission spectra.

The photovoltaic properties of the solar cells were characterized using a VeraSol LSH-7520 LED solar simulator, which was classified as AAA according to IEC 60904-9 standards. The key photovoltaic parameters short-circuit current density (J_{SC}), open-circuit voltage (V_{OC}), fill factor (FF), and power conversion efficiency (PCE) were measured. Additionally, the simulator allowed measurements under varying light intensities, effectively simulating real-world operational conditions. Data acquisition and analysis were performed using LabVIEW-based software, ensuring precision and streamlined workflows.

External quantum efficiency (EQE) measurements were performed using a Newport QUANTX-300 system for precise spectral response characterization over 320-1800 nm. The measurements were conducted at room temperature, with the system equipped with light biasing, electrical probing, and a lock-in amplifier for stable signal acquisition. The EQE measurements were performed over the wavelength range of 350 to 800 nm.

4 RESULTS AND DISCUSSION

The $NaGdF_4$:Yb^{3+},Er^{3+} and $NaGdF_4$:Yb^{3+},Tm^{3+} core NPs were synthesized via a thermolysis approach. Typical TEM micrographs of β-$NaGdF_4$:Yb^{3+},Er^{3+} and β-$NaGdF_4$:Yb^{3+},Tm^{3+} NPs reveal that both exhibit a similar quasi-spherical morphology, as illustrated in Figures 9a and 10a. Furthermore, size distribution histograms derived from these micrographs (Figures 9b and 10b) indicate average particle diameters of 12.0 ± 1.0 nm for β-$NaGdF_4$:Yb^{3+},Er^{3+} and 12.5 ± 1.0 nm for β-$NaGdF_4$:Yb^{3+},Tm^{3+}, respectively.

Figure 9 – Characterization of the $NaGdF_4$:Yb,Er core: (a) TEM image, (b) size distribution from TEM with an average size of approximately 12 nm, (c) XRD pattern, and (d) photoluminescence spectrum.

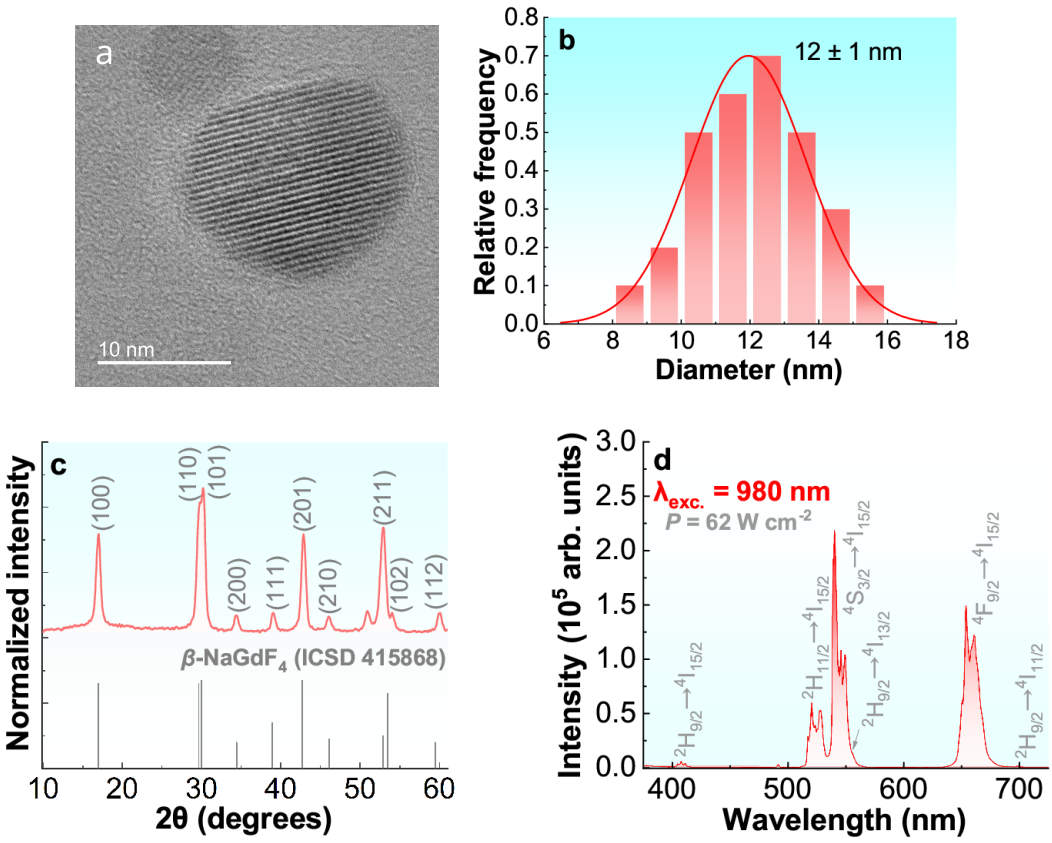

Source: Palácio *et al.*, 2025 (82).

To assess the effect of inert shell growth, the corresponding core–shell nanoparticles were analyzed, as shown in Figures 11b and 11c. A noticeable increase in particle size was observed after shell deposition: the Er^{3+} and Tm^{3+} based core–shell NPs reached average

diameters of 19.0 ± 1.0 nm (ERN) and 16.0 ± 1.0 nm (TMN), respectively. These values correspond to estimated shell thicknesses of approximately 3.5 nm for ERN and 1.8 nm for TMN, confirming successful and uniform shell growth in both systems, with a more substantial shell observed in the Er^{3+}-doped nanoparticles.

Figure 10 – Characterization of the $NaGdF_4$:Yb,Tm core: (a) TEM image, (b) size distribution from TEM with an average size of approximately 12.5 nm, (c) XRD pattern, and (d) photoluminescence spectrum.

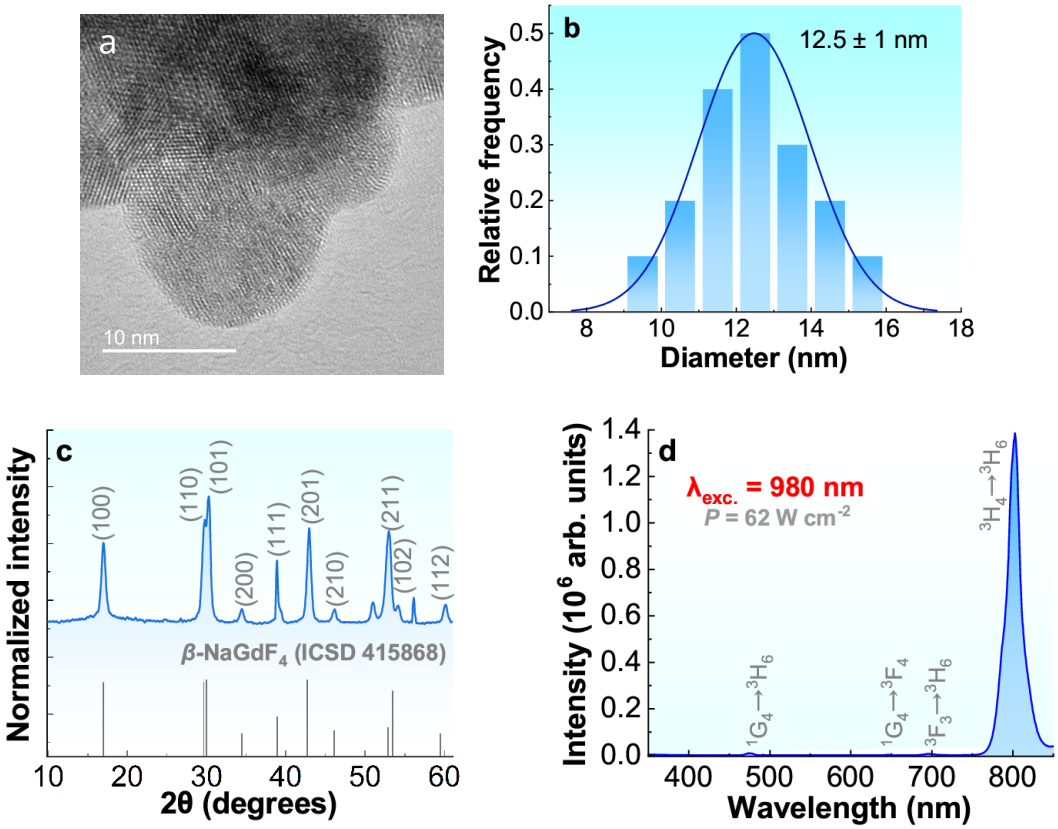

Source: Palácio *et al.*, 2025 (82).

Figures 9c and 10c present the XRD patterns of both cores, which exhibit diffraction peaks corresponding to a hexagonal crystal structure (space group $P6_3/m$), as referenced in the ICSD 415868 file card. These patterns were indexed to the crystallographic planes (100), (110), (101), (200), (111), (201), (211), (102), and (112), confirming the β-phase of the $NaGdF_4$:Yb^{3+},Er^{3+} and $NaGdF_4$:Yb^{3+},Tm^{3+} NPs. The results are consistent with previous reports in the literature (25, 77).

The photoluminescence spectra in the visible region, acquired under 980 nm excitation (62 W cm^{-2}), are shown in Figures 9d and 10d. The emission process originates from the excitation of Yb^{3+} ions, attributed to the $^2F_{7/2}$ to $^2F_{5/2}$ transition. This is followed by energy transfer to Tm^{3+} and Er^{3+} ions (83), albeit through distinct pathways. In the $NaGdF_4$:Yb^{3+},Er^{3+} NPs (Figure 9d), characteristic emission lines were observed, corresponding to the transitions $^2H_{9/2} \rightarrow {}^4I_{15/2}$ (408 nm), $^2H_{11/2} \rightarrow {}^4I_{15/2}$ (528 nm), $^4S_{3/2} \rightarrow {}^4I_{15/2}$ (550 nm), $^4F_{9/2} \rightarrow {}^4I_{15/2}$ (661 nm) and $^2H_{9/2} \rightarrow {}^4I_{11/2}$ (698 nm) consistent with previous reports (35). Conversely, the $NaGdF_4$:Yb^{3+},Tm^{3+} NPs (Figure 10d) exhibited typical emissions from the transitions $^1G_4 \rightarrow {}^3H_6$ (476 nm), $^1G_4 \rightarrow {}^3F_4$ (645 nm), $^3F_3 \rightarrow {}^3H_6$ (696 nm) and $^3H_4 \rightarrow {}^3H_6$ (800 nm), as documented in the literature (23). These results confirm the upconversion properties of the core NPs.

Figure 11 illustrates the structural and morphological characteristics of core-shell β-$NaGdF_4$-based NPs doped with Yb^{3+}/Er^{3+} (ERN) and Yb^{3+}/Tm^{3+} (TMN), coated with a Eu^{3+}-doped shell. The XRD patterns shown in Figure 11a confirm the presence of the hexagonal β-phase in both samples, with peaks aligning to the reference from ICSD 415868 and indexed to the characteristic planes (100), (110), (101), among others (84). The particles display a monodisperse size distribution, as indicated by the minimal error in the average diameters obtained from TEM images (Figures 11b and 11c). The histograms show average diameters of 19.0 ± 1.0 nm for ERN and 16.0 ± 1.0 nm for TMN, corresponding to a $NaGdF_4$:Eu^{3+} shell thickness of 3.5 and 1.8 nm, respectively. Suggesting that adding a shell of $NaGdF_4$:Eu^{3+} to the core increased the overall size of NPs in a few nanometers. Furthermore, the SAED patterns corroborate the XRD data, reinforcing the hexagonal crystalline structure by indexing the rings to the defining lattice planes of β-$NaGdF_4$. These findings confirm the successful synthesis of highly crystalline, monodisperse NPs with controlled size and high phase purity.

The synthesized ERN exhibits upconversion emission via well-established energy transfer between Yb^{3+} and Er^{3+}. The emission bands observed correspond to the transitions $^2H_{9/2} \rightarrow {}^4I_{15/2}$ (408 nm), $^2H_{11/2} \rightarrow {}^4I_{15/2}$ (520 nm), $^4S_{3/2} \rightarrow {}^4I_{15/2}$ (540 nm), $^2H_{9/2} \rightarrow {}^4I_{13/2}$ (556 nm), $^4F_{9/2} \rightarrow {}^4I_{15/2}$ (654 nm), and $^2H_{9/2} \rightarrow {}^4I_{11/2}$ (698 nm) of Er^{3+}, upon excitation with a 980 nm continuous-wave laser diode (Figure 12a) (85–87). Moreover, emission bands corresponding to the $^5D_0 \rightarrow {}^7F_1$ and $^5D_0 \rightarrow {}^7F_2$ transitions of Eu^{3+} were also detected, peaking at 590 nm and 615 nm, respectively. It is crucial to note that, despite these Eu^{3+} emission bands being excited by 980 nm radiation, Eu^{3+} ions do not absorb near-infrared photons. Consequently, the observed emissions must originate from the energy transfer between Er^{3+} and Eu^{3+} (88, 89).

Figure 11 – Structural and morphological characterization of β-$NaGdF_4$-based NPs. (a) XRD patterns confirm the hexagonal β-phase for ERN (red) and TMN (blue), matching the ICSD 415868 reference. (b, c) TEM images show well-dispersed NPs with average diameters of 19 ± 1 nm for ERN (b) and 16 ± 1 nm for TMN (c). Insets: particle size distributions and SAED patterns confirming crystallinity.

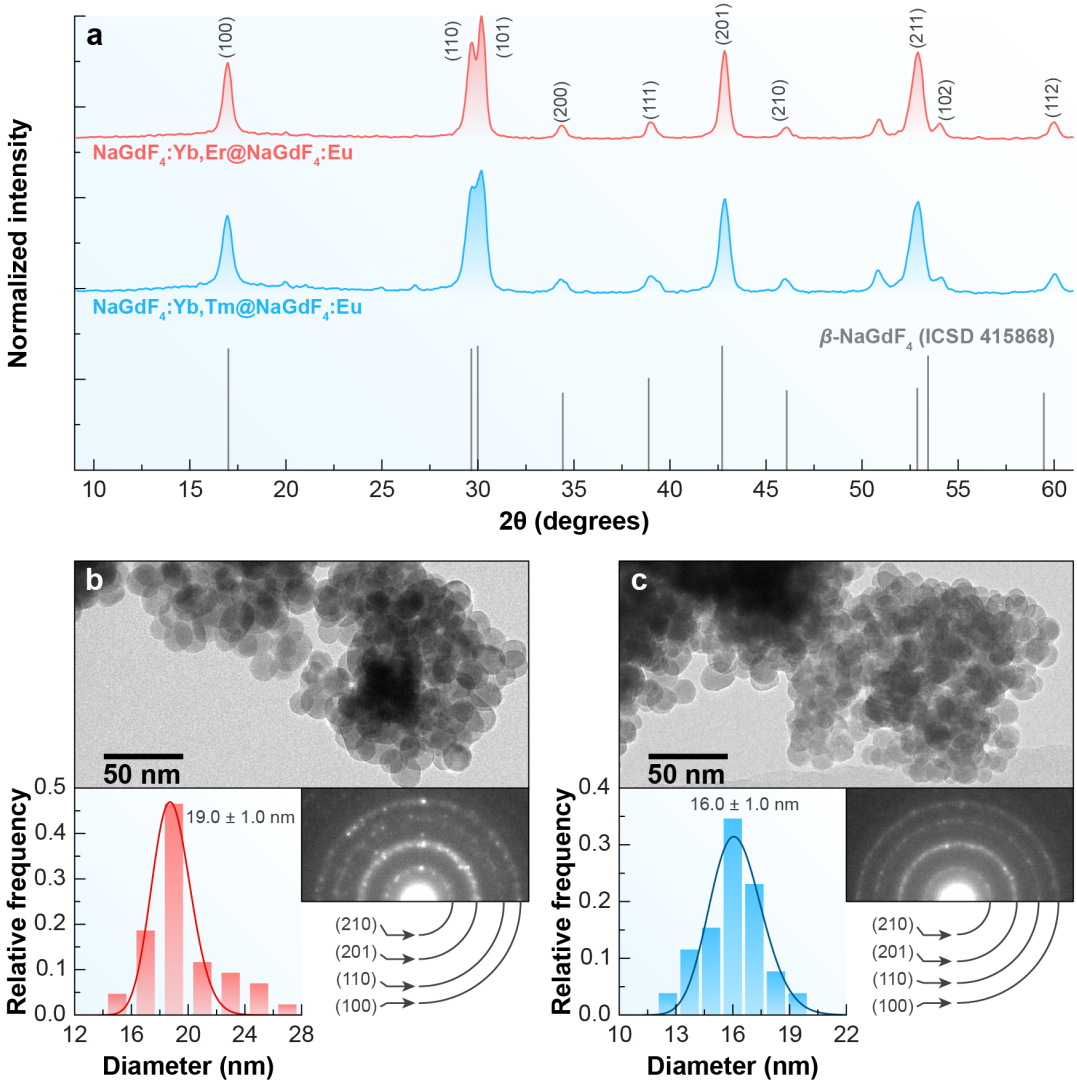

Source: Palácio *et al.*, 2025 (82).

When the energy gap between the $^4S_{3/2}$ (Er^{3+}) and $^5D_0$ (Eu^{3+}) levels is approximately 1,000 cm^{-1}, and the $^2H_{11/2}$ (Er^{3+}) and $^5D_1$ (Eu^{3+}) levels are nearly overlapping, energy transfer from Er^{3+} to Eu^{3+} becomes feasible (90), as illustrated in Figure 12b. Moreover, both the emission profile and the lifetime of Eu^{3+} remain constant, regardless of whether direct excitation at 395 nm or Yb^{3+}-mediated excitation at 980 nm is employed, as observed in Figures 13a and 13b.

Figure 12 – Optical characterization of ERN (Er^{3+}). (a) Upconverting emission spectra under 980 nm. (b) Partial energy level diagram depicting the energy transfer pathway between Yb^{3+}, Er^{3+}, and Eu^{3+}. The solid lines indicate radiative transitions, curly arrows display nonradiative decays, and dotted lines represent nonradiative energy transfer. (c) Excitation spectrum monitoring the emission at 615 nm (left) and downshifting emission spectra under 274 and 395 nm excitation (right).

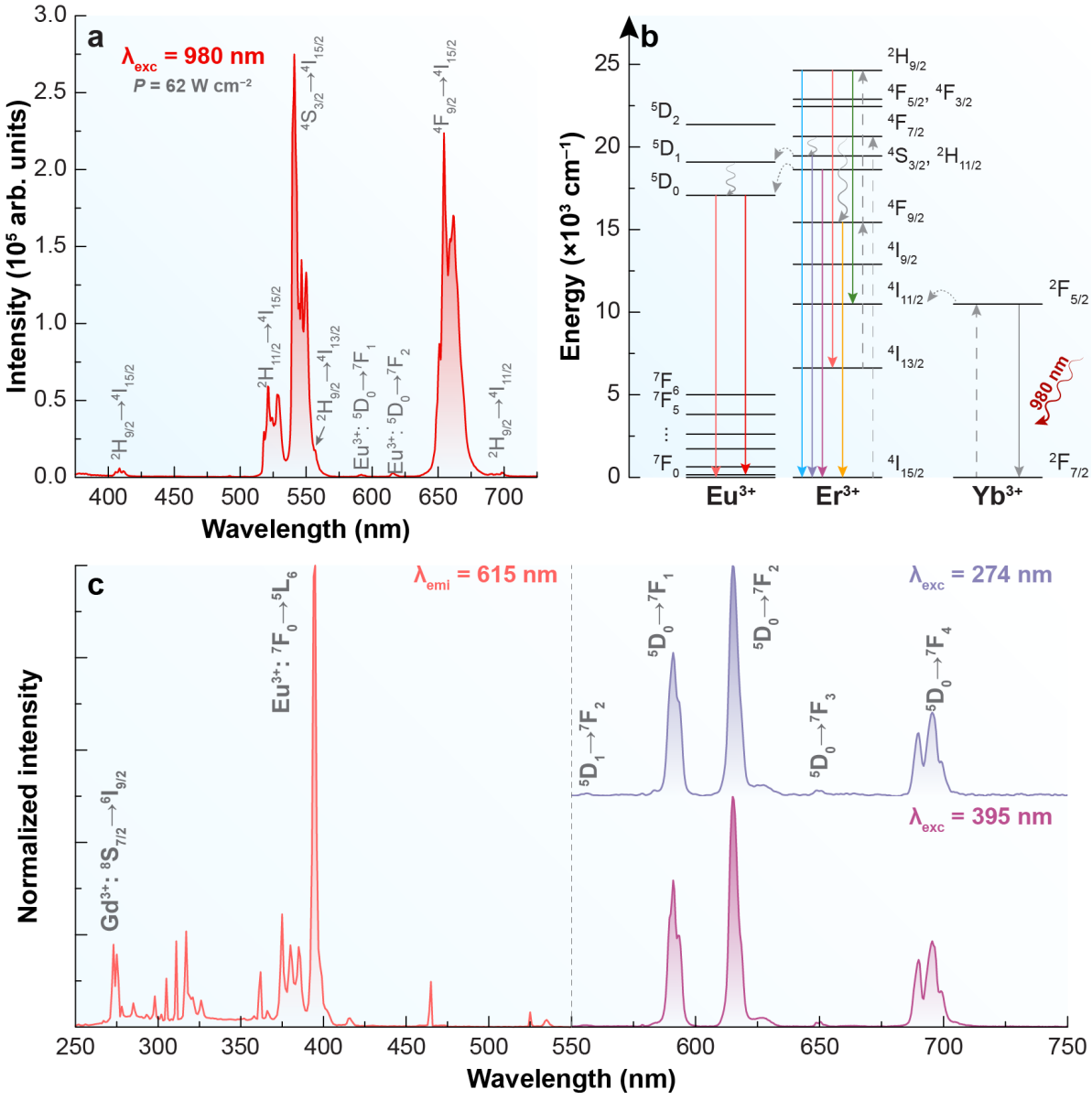

Source: Palácio *et al.*, 2025 (82).

Figure 13 – Optical characterization of ERN (Eu^{3+}). (a) Emission spectra of the ERN under excitation at 395 nm (Eu^{3+}, blue) and 980 nm (Er^{3+}, red). (b) Emission decay profiles of the $^5D_0$ emitting level of Eu^{3+} under excitation at 395 nm and 980 nm, monitoring the emission at 615 nm. The symbols represent the experimental data, and the solid lines correspond to the best-fitting monoexponential curves, with the calculated $^5D_0$ lifetime ($\tau_{^5D_0}$). (c) Upconverting emission spectra of ERN under 980 nm excitation at varying excitation power P. (d) Double logarithmic plot of the integrated intensities I of the $^5D_0 \rightarrow {}^7F_2$ (Eu^{3+}, 609–622 nm) and $^4F_{9/2} \rightarrow {}^4I_{15/2}$ (Er^{3+}, 635–685 nm) emission bands from panel (c), indicating the corresponding number of photons n.

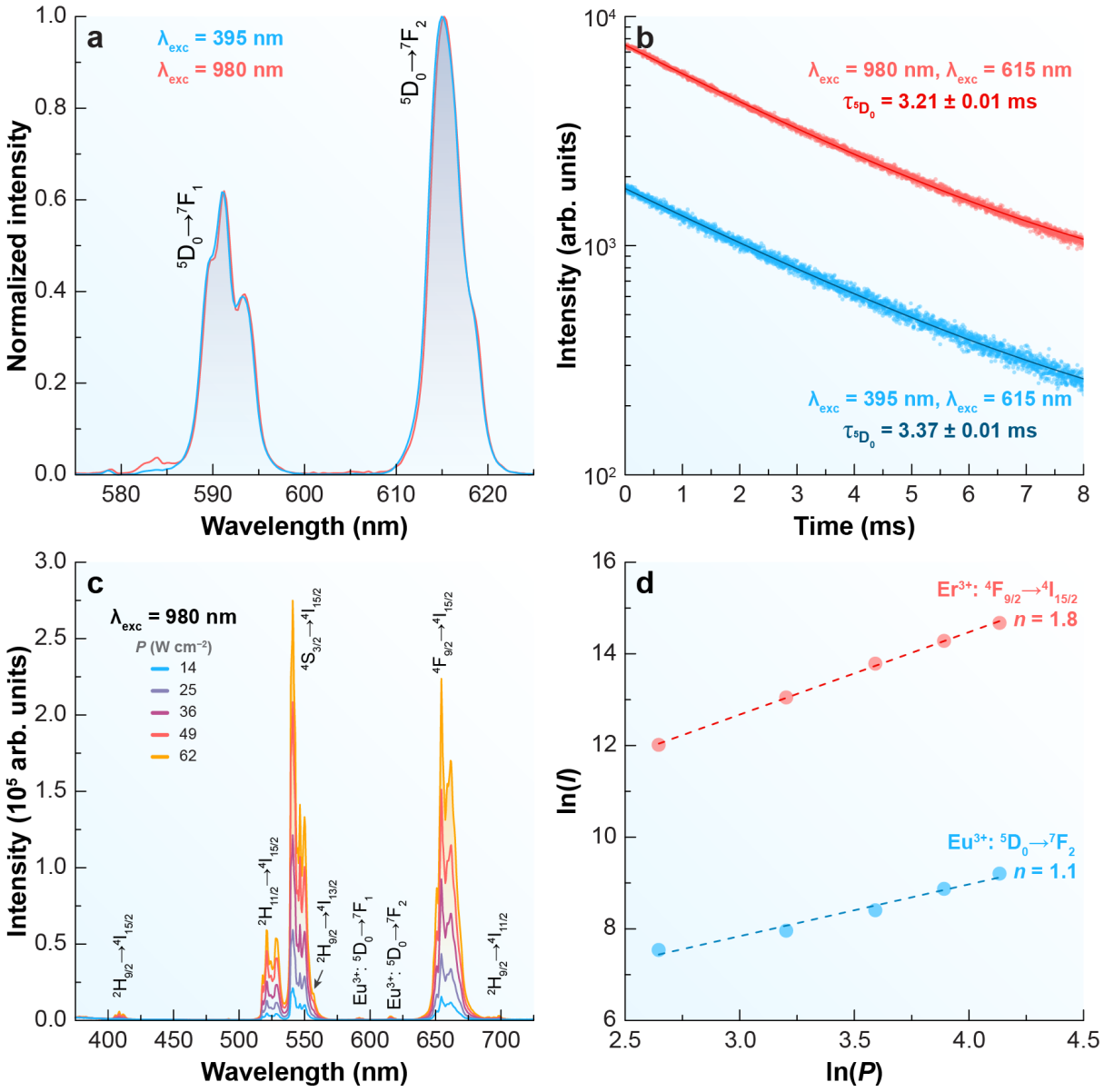

Source: Palácio *et al.*, 2025 (82).

A straightforward approach to demonstrate upconversion in materials doped with Yb/Er or Yb/Tm ion pairs is by analyzing the power (P) dependence of the emitted intensity (I). Because upconversion is a non-linear process, the emission follows a power law, $I \propto P^n$, where n corresponds to the number of absorbed photons (91). For the ERN sample, the Er^{3+} emission ($^4F_{9/2} \rightarrow ^4 I_{15/2}$, peaking at 654 nm) displays $n = 1.8$, confirming that upconversion is indeed the mechanism behind Er^{3+} emission. In contrast, the Eu^{3+} emission ($^5D_0 \rightarrow ^7 F_2$, peaking at 615 nm) observed under 980 nm excitation shows $n = 1.1$ (Figures 13c–d). Although this slope is close to unity, the process must still be regarded as upconversion, since NIR excitation produces visible Eu^{3+} emission. The low slope value reflects that the emission originates from $Er^{3+} \rightarrow Eu^{3+}$ energy transfer rather than from direct multiphoton absorption by Eu^{3+} ions. This interpretation is further supported by the emission lifetimes and spectral profiles recorded under 395 and 980 nm excitation (Figures 13a–b), which are nearly identical, confirming that the observed signal originates from Eu^{3+} emission. Regardless of the excitation pathway, the same emission profile (peak positions and full width at half maximum) is observed, giving rise to characteristic Eu^{3+} emission bands, including $^5D_1 \rightarrow ^7F_2$ (556 nm) and $^5D_0 \rightarrow ^7F_{J=1-4}$ (590, 615, 650, 696 nm) (92). While both upconversion and downshifting processes have been identified for TMN, no evidence of energy transfer from Tm^{3+} to Eu^{3+} was observed (see Figure 14).

Eu^{3+} emission can be activated under different excitation pathways. Under NIR excitation (980 nm), it arises from Er^{3+}-mediated upconversion, while under UV excitation it can result either from direct Eu^{3+} absorption ($^7F_0 \rightarrow ^5L_6$, 395 nm) or from Gd^{3+}-mediated transfer ($^8S_{7/2} \rightarrow ^6I_{9/2}$, 274 nm) (93), as illustrated in Figure 12c.

In short, Eu^{3+} emission in the ERN sample arises from a dual mechanism:Er^{3+}-triggered upconversion under NIR excitation and direct/indirect excitation (via Eu^{3+} or Gd^{3+}) under UV excitation. This combination enables the efficient harvesting of both the UV and NIR regions of the solar spectrum, representing a significant advantage for enhancing solar cell performance.

Although steady-state emission intensities measured under 980 nm excitation remained similar between core and core–shell samples (Figure 15), the substantial enhancement in PLQY confirms a more efficient radiative process in the core–shell structure.

In contrast, the TMN nanoparticles exhibited a decrease in PLQY upon shell growth (from 0.35% to 0.024% at 944.2 W cm^{-2}), indicating that the shell may have introduced additional nonradiative pathways or hindered energy transfer. Nonetheless, the TMN core–shell

Figure 14 – Optical characterization of TMN (Tm^{3+}). (a) Upconverting emission spectra under 980 nm excitation at varying power densities *P*. (b) Partial energy level diagram depicting the energy transfer pathway between Yb^{3+} and Tm^{3+}. The solid lines indicate radiative transitions, curly arrows display nonradiative decays, and dotted lines represent nonradiative energy transfer. (c) Excitation spectrum monitoring the emission at 615 nm (left) and downshifting emission spectra under 274 and 395 nm excitation (right).

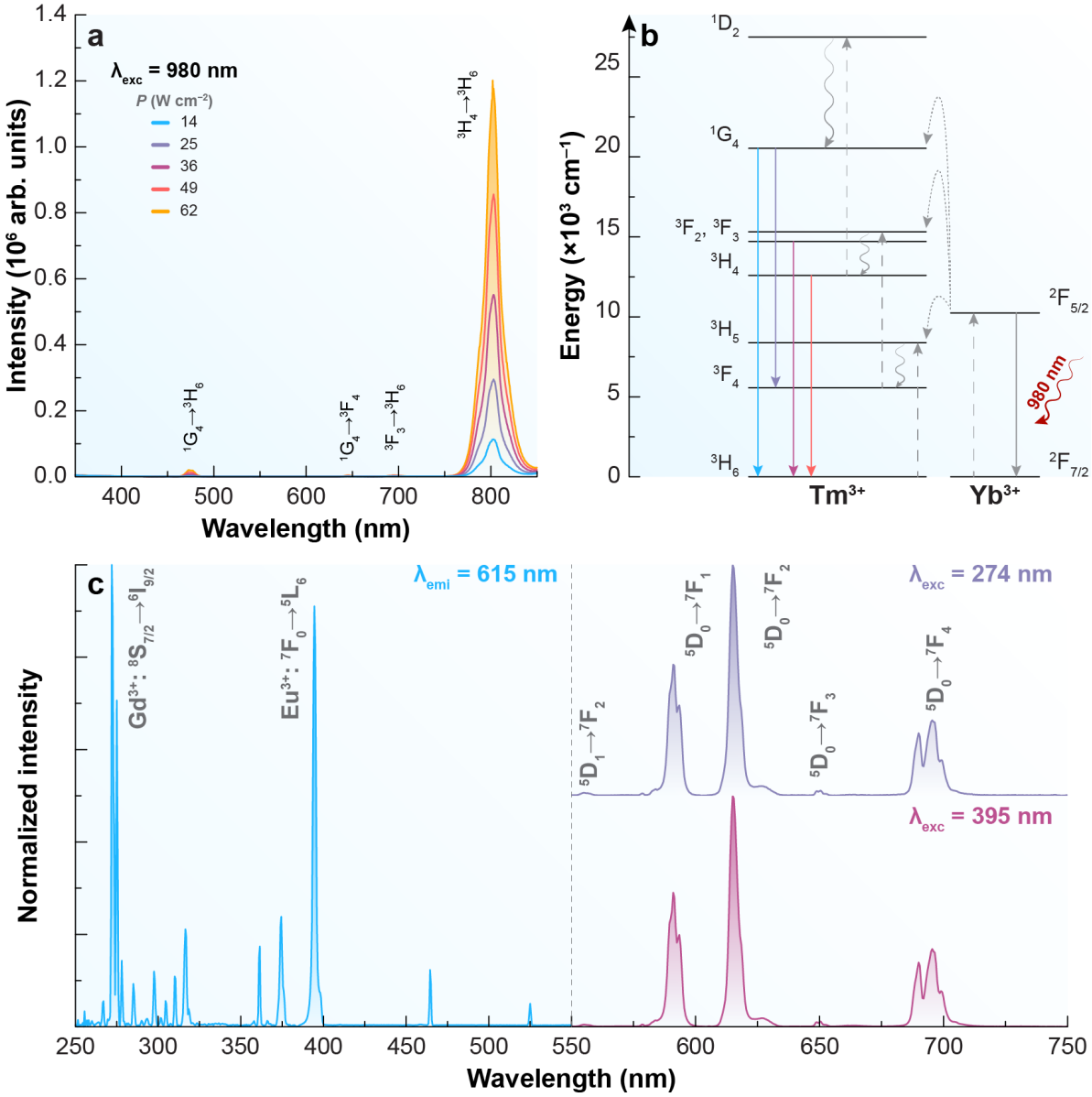

Source: Palácio *et al.*, 2025 (82).

Figure 15 – Emission of: (a) ERN core ($NaGdF_4$:Yb,Er) and ERN core-shell ($NaGdF_4$:Yb,Er@$NaGdF_4$:Eu) and (b) TMN core ($NaGdF_4$:Yb,Tm) and TMN core-shell ($NaGdF_4$:Yb,Tm@$NaGdF_4$:Eu).

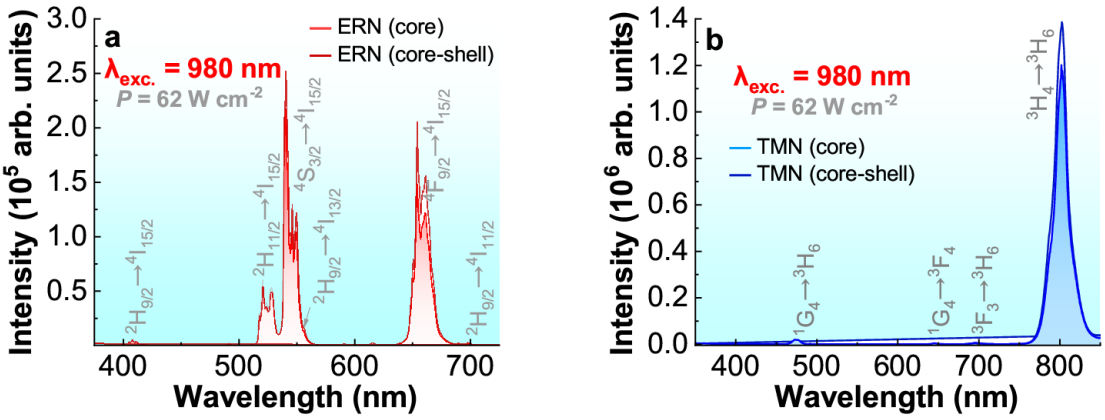

Source: Palácio *et al.*, 2025 (82).

sample exhibited strong emission under UV excitation (274 and 395 nm), which is relevant for downshifting (Figure 14). Therefore, despite the differing behaviors, the core–shell architecture was preferred for device integration due to its superior PLQY and luminescent performance under practical excitation conditions.

In this study, upconversion was considered as a complementary mechanism to downshifting, aiming to broaden the absorption spectrum of perovskite solar cells (PSCs) and potentially enhance their efficiency. Downshifting alone converts high-energy photons into wavelengths more efficiently absorbed by the perovskite layer. In contrast, upconversion enables NIR sub-bandgap photons to be converted into higher-energy photons usable by the active layer. This synergistic combination allows for more comprehensive harvesting of the solar spectrum. Although previous studies have demonstrated that core/shell architectures can enhance downshifting photoluminescence quantum yield (PLQY) through surface passivation, the primary goal of the present work was to investigate the role of these multiple luminescent properties in potentially improving PSC performance.

Table 2 presents the quantum yield (QY) values for different excitations for core and core–shell architecture NPs, highlighting the best result obtained for the ERN sample in powder form, with a QY of 16.41% when excited at 395 nm in Eu^{3+}. This high value reflects the efficiency of downshifting processes, which enhance light absorption in the visible region (94).

Only the core–shell nanoparticles were incorporated into PSCs, as they exhibited significantly higher photoluminescence quantum yields (PLQY) compared to their core-only counterparts under relevant excitation conditions (Table 2). For instance, the PLQY of ERN increased nearly 300-fold, from 0.0001% (core) to 0.0291% (core–shell) under 980 nm excitation at 1862.6 W cm^{-2}. This improvement is attributed to the passivating effect of the shell, which mitigates nonradiative recombination by shielding Yb^{3+} and Er^{3+} ions at the nanoparticle surface and reducing surface defect density (95).

Table 2 – Quantum yield values of ERN and TMN samples under different excitation conditions and power densities.

Samples	**Excitation (nm)**	**Power density (W cm^{-2})**	**QY (%)**
ERN (core)	980	944.2	0.0001
	980	1862.6	0.0019
ERN (core-shell)	274	-	7.7600
	395	-	16.4100
	980	944.2	0.0001
	980	1862.6	0.0291
TMN (core)	980	944.2	0.3500
TMN (core-shell)	274	-	5.1300
	395	-	7.8300
	980	944.2	0.0240

Source: Palácio *et al.*, 2025 (82).

Figure 16a shows J-V curves for the control and ERN-bearing devices, highlighting the significant increase in power conversion efficiency in the ERN device (14.50%) compared to the control (11.90%). The device architecture in the inset features the glass/ITO/NiO_x/NPs/Perovskite/PCBM/BCP/Ag layers optimized to maximize charge-carrier extraction and

transport. The superior performance of the ERN device can be attributed to two main factors: (i) the high QY of 16.41% obtained for excitation at 395 nm, reflecting efficient downshifting processes (38, 96), and (ii) the passivation effect provided by the ERN NPs. Passivation reduces structural defects, minimizing non-radiative recombination of charge carriers (97–99). The ERN NPs are also expected to enhance light scattering within the cell, thereby improving optical absorption. The improved performance of the ERN-based device is primarily attributed to the efficient downshifting emission of the nanoparticles, as demonstrated by the relatively high photoluminescence quantum yield (PLQY) of 16.41% under 395 nm excitation (38, 96). This downshifting process enhances spectral overlap with the perovskite absorption, thereby increasing photon harvesting. Additionally, the ERN nanoparticles may increase light scattering within the device, thereby increasing optical path length and further improving light absorption. Although a passivation effect is often considered beneficial in nanostructured materials (97–99), in this case, its contribution to device performance is expected to be limited, given the low upconversion PLQY (< 0.1%), which reduces its direct impact under operational conditions.

Figure 16 – Electrical and optoelectrical characterizations of the PSCs. (a) J-V curves of the best solar cells of the photovoltaic prototype, after incorporating ERN, compared to those of a control device. The inset shows the architecture of the fabricated prototype. (b) The EQE spectrum of the best solar cells of the device containing ERN compared with that of the control device.

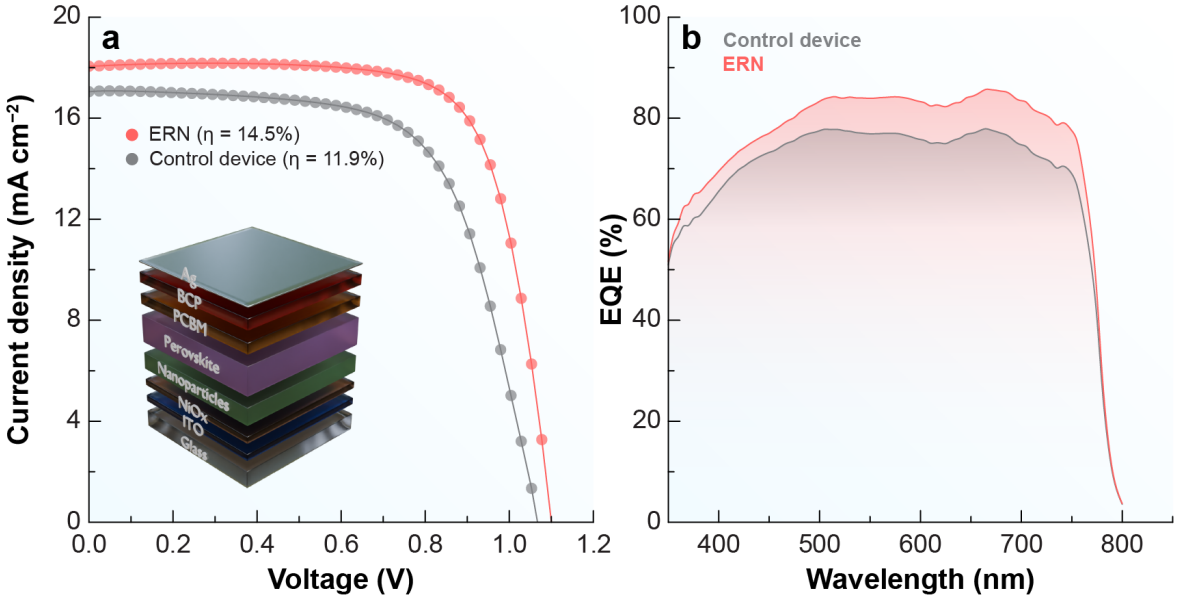

Source: Palácio *et al.*, 2025 (82).

External quantum efficiency spectra are presented in Figure 16b. It can be observed that the ERN device consistently shows higher EQE values across the analyzed spectral range, particularly in the visible region, where the ERN NPs promote more efficient conversion of incident light. These results support improved photogenerated charge extraction, driven by defect passivation and optimized device-layer interfaces.

Interestingly, while the high QY at 395 nm indicates greater efficiency in photon absorption and re-emission in the visible region, the difference in EQE suggests additional contributions to the increase in PCE beyond the optical gain provided by downshifting. The device architecture, which integrates the NPs at the interface between NiO_x and the perovskite layer, plays a crucial role in this process, maximizing charge-carrier collection and reducing losses from non-radiative recombination.

Figure 17 illustrates the effect of incorporating ERN on the photovoltaic parameters of ten perovskite solar cells within a photovoltaic device, including the cell with the highest PCE depicted in Figure 16. The parameters analyzed are open-circuit voltage (Figure 17a, V_{OC}), short-circuit current density (Figure 17b, J_{SC}), fill factor (Figure 17c, FF), and power conversion efficiency (Figure 17d, PCE). Each graph compares ERN-containing cells with control cells, revealing significant improvements in the performance of the ERN-containing cells.

The observed increase in V_{OC} is likely a result of enhanced charge separation or reduced recombination losses at the interface (100). These findings suggest that ERN NPs effectively act as a passivation layer, promoting beneficial electronic interactions with the perovskite material (71). The improvement in J_{SC} values can be attributed to enhanced light absorption through two distinct mechanisms: (i) efficient light conversion facilitated by the downshifting properties of the NPs, which expand the absorption spectrum (38, 96), and (ii) increased light scattering within the device, which leads to a more effective utilization of the incident light. Additionally, more efficient charge transport and reduced non-radiative recombination losses (97–99) also contribute to the observed performance improvement. Additionally, the rise in FF suggests that incorporating ERN into the cells reduces series resistance or enhances interfacial contact between device layers, facilitating more effective charge extraction and transport (101). The increase in PCE is a consequence of the combined enhancements in V_{OC}, J_{SC}, and FF, implying that ERN NPs contribute to improving overall device performance through potential synergistic effects on light harvesting, charge carrier dynamics, and interface passivation (67, 102).

Figure 17 – Photovoltaic performance of PSCs with (ERN) and without (Control) the addition of ERN. (a) Open-circuit voltage (V_{OC}), (b) short-circuit current density (J_{SC}), (c) fill factor (FF), and (d) power conversion efficiency (PCE).

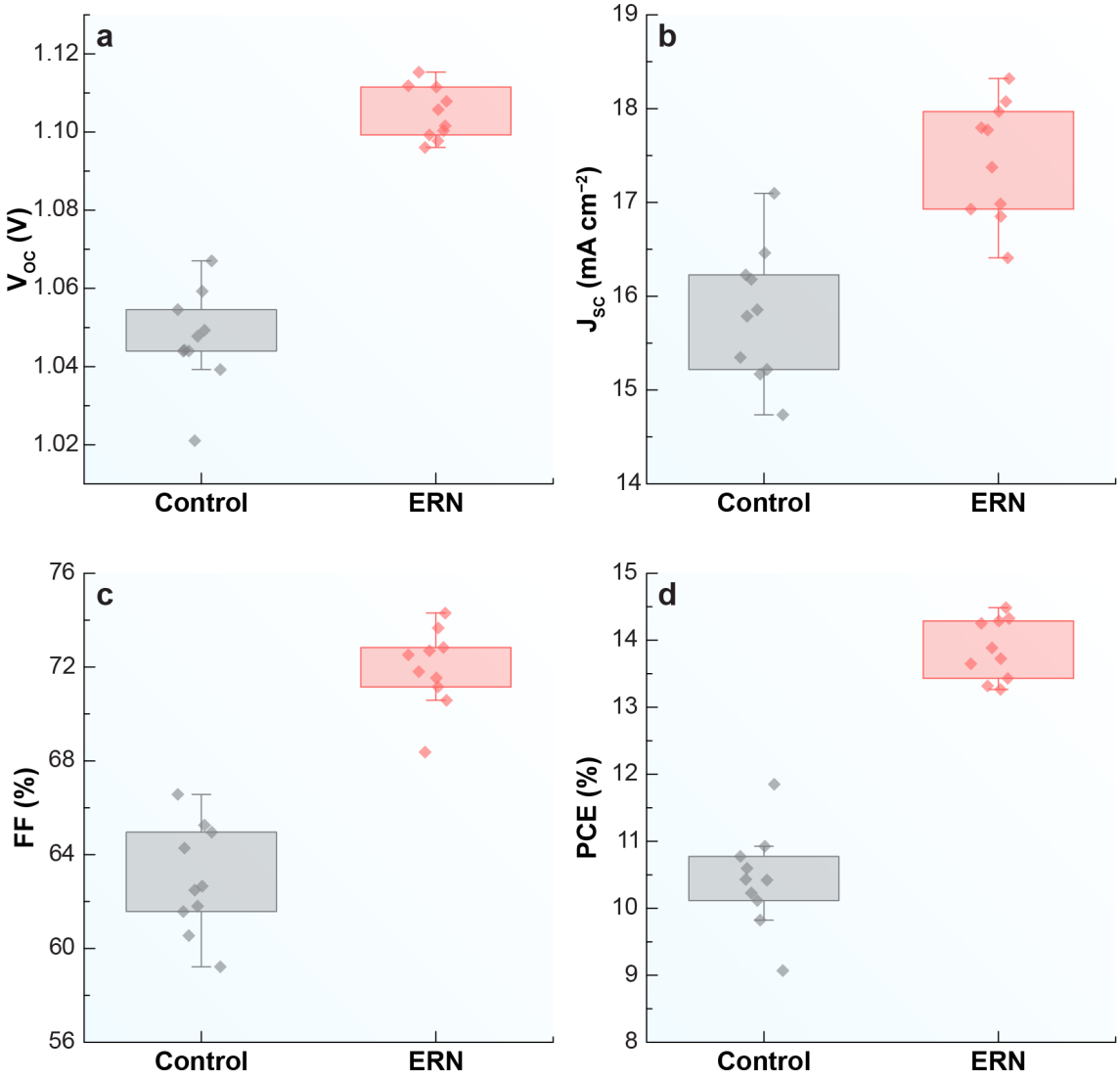

Source: Palácio *et al.*, 2025 (82).

The photovoltaic performance of the PSCs with and without TMN incorporation is summarized in Figure 18. The power conversion efficiency (PCE) of the best-performing devices increased from 13.0% for the control device to 14.7% for the TMN-based device, as shown in Figure 19a. Despite this improvement in PCE, no significant changes were observed in the open-circuit voltage (V_{OC}) or fill factor (FF), suggesting that the performance enhancement is primarily attributed to increased current generation or improved charge transport.

Figure 18 – Photovoltaic performance of PSCs with (TMN) and without (Control) the addition of TMN. (a) Open-circuit voltage (V_{OC}), (b) short-circuit current density (J_{SC}), (c) fill factor (FF), and (d) power conversion efficiency (PCE).

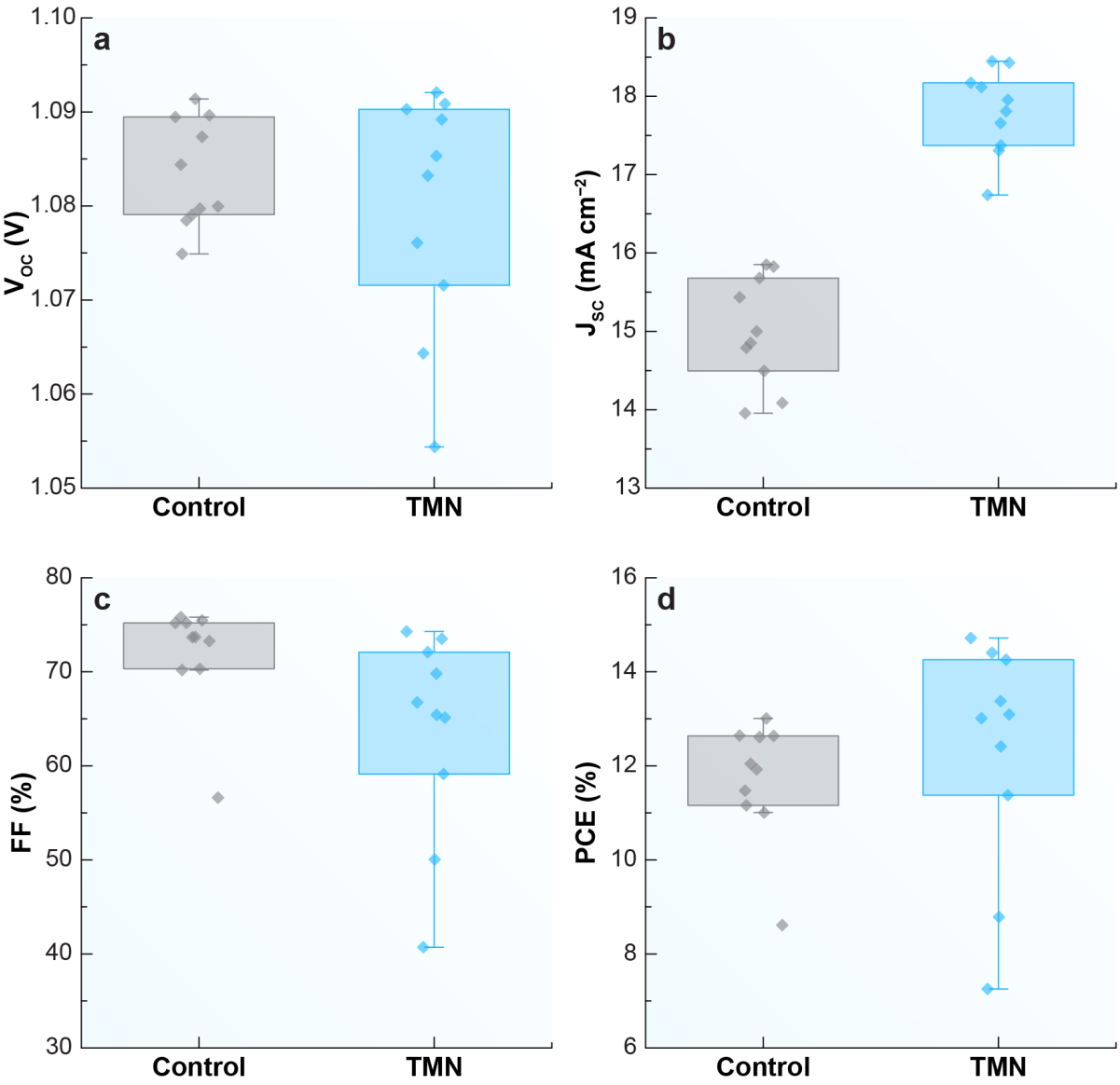

Source: Palácio *et al.*, 2025 (82).

These findings are consistent with the J–V curves presented in Figure 19a, where the TMN-based device exhibits a slightly higher current density compared to the control. Furthermore, the external quantum efficiency (EQE) spectra shown in Figure 19b indicate a broader and more efficient photon harvesting in the TMN-incorporated devices, particularly across the visible region. This enhanced light absorption likely contributes to the observed increase in PCE.

Figure 19 – Electrical and optoelectrical characterizations of the PSCs. (a) J-V curves of the best solar cells of the photovoltaic prototype, after incorporating TMN, compared to those of a control device. (b) The EQE spectrum of the best solar cells of the device containing TMN compared with that of the control device.

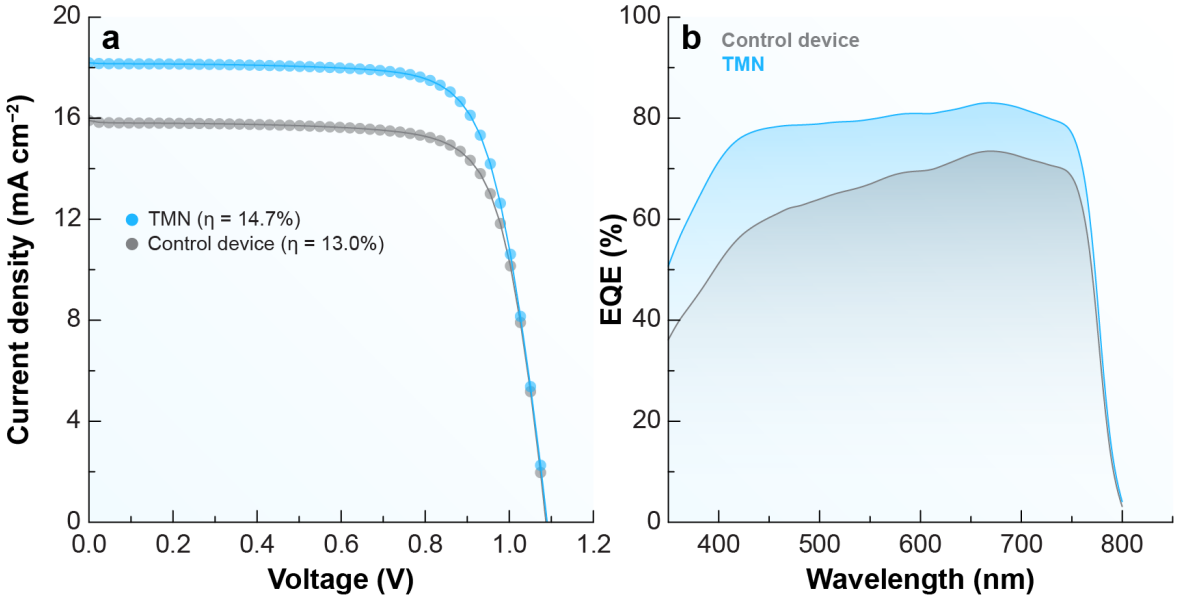

Source: Palácio *et al.*, 2025 (82).

In contrast, ERN-based PSCs exhibited superior performance across all key photovoltaic parameters. This enhancement is mainly due to the higher photoluminescence quantum yield (PLQY) of the Eu^{3+}-doped shell under 395 nm excitation, which significantly boosts downshifting efficiency by converting high-energy photons into wavelengths better absorbed by the perovskite. Moreover, the thicker shell in ERN nanoparticles (3.5 nm vs. 1.8 nm for TMN) not only improves surface passivation, effectively reducing non-radiative recombination losses, but also stabilizes the Eu^{3+} ions responsible for downshifting emission. The synergistic effect of enhanced photon conversion and reduced recombination leads to a notable improvement in photovoltaic performance observed in ERN-containing devices.

5 CONCLUSION AND FUTURE WORK

5.1 Conclusion

The incorporation of ERN and TMN NPs in PSC devices has significantly influenced their photovoltaic performance. Although these nanoparticles are known for their upconversion and downshifting optical properties, the contribution of upconversion-capable NPs to photovoltaic efficiency remains to be confirmed. Further investigation is needed to determine the extent of their beneficial effects. Additionally, these NPs have broadened the spectral response of PSCs, enhancing light absorption and potentially improving overall device efficiency. Specifically, PSCs containing ERN exhibited a 22.19% increase in power conversion efficiency, achieving 14.50% compared to the control cells, which reached 11.90%. This improvement can be attributed to the high efficiency of the downshifting process of the ERN NPs, which demonstrated an absolute quantum yield of 16.41% when excited at 395 nm. Additionally, morphological aspects may have played a crucial role: ERN NPs possess a thicker shell (3.5 nm) than TMN NPs (1.8 nm), which can provide more effective surface passivation and reduce non-radiative recombination, thereby further enhancing device performance.

The presence of TMN also contributed to an increase in power conversion efficiency, though the relative improvement was more modest at 13.23%. This more limited enhancement may be related not only to differences in optical properties but also to the thinner shell structure of TMN NPs, which may result in less efficient surface passivation.

Moreover, key photovoltaic parameters, including open-circuit voltage, short-circuit current density, and fill factor, were enhanced by the addition of NPs. This enhancement may be linked to the passivation of interfaces and a reduction in non-radiative recombination losses. However, it remains unclear whether these enhancements are primarily related to the photonic properties of the NPs, their structural attributes, the interplay of multiple factors, or other mechanisms, such as solvent effects and surface passivation. Further research is necessary to determine whether the improvements stem from photophysical processes, such as enhanced photon conversion or modifications to device architecture. Additionally, the long-term stability of the cells and the investigation of new doping compositions warrant exploration in future studies to assess the ongoing advancement of photovoltaic technologies.

5.2 Future Work

- Investigate synthesis routes of lanthanide fluoride nanoparticles with core and core-shell structures, identifying the most suitable one through characterization techniques such as X-ray diffraction, electron microscopy, and spectroscopy in Fourier-transform infrared, ultraviolet–visible, Raman, and photoluminescence;
- Explore surface functionalization of nanoparticles and define the best route for dispersion production, employing techniques such as dynamic light scattering;
- Deposit thin films combining materials typically used in the active layers of organic solar cells (low-bandgap polymers and small molecules with high electron affinity) and nanoparticles, determining the optimal deposition conditions with the aid of techniques such as electron microscopy and atomic force microscopy;
- Evaluate the effects of nanoparticle incorporation into the active layers of organic solar cells, assessing their contribution to the enhancement of the absorbed solar spectrum fraction through ultraviolet–visible and photoluminescence spectroscopy;
- Elucidate the mechanisms of exciton generation and diffusion.

REFERENCES

1 ZEI, S. Developments and barriers in solar energy: conversion technologies, system integration, and future directions. **Energy Conversions**, Amsterdam, v. 1, 2025.

2 IEA. **Global energy review 2025: electricity**. Paris, 2025. Available at: https://www.iea.org/reports/global-energy-review-2025/electricity. Accessed on: 22 Oct. 2025.

3 LIU, X.; ZHANG, J.; TANG, L.; GONG, J.; LI, W.; MA, Z.; TU, Z.; LI, Y.; LI, R.; HU, X. *et al.* Over 28% efficiency perovskite/Cu (InGa)Se_2 tandem solar cells: highly efficient sub-cells and their bandgap matching. **Energy & Environmental Science**, London, v. 16, n. 11, p. 5029–5042, 2023.

4 ZHANG, X.; WU, S.; ZHANG, H.; JEN, A. K.; ZHAN, Y.; CHU, J. Advances in inverted perovskite solar cells. **Nature Photonics**, London, v. 18, n. 12, p. 1243–1253, 2024.

5 XU, C.; HANG, P.; KAN, C.; GUO, X.; SONG, X.; XU, C.; YOU, G.; LIAO, W.-Q.; ZHU, H.; WANG, D.; CHEN, Q.; HONG, Z.; XIONG, R.-G.; YU, X.; ZUO, L.; CHEN, H. Molecular ferroelectric self-assembled interlayer for efficient perovskite solar cells. **Nature Communications**, London, v. 16, n. 1, p. 835, 2025.

6 GREEN, M. A.; BREMNER, S. P. Energy conversion approaches and materials for high-efficiency photovoltaics. **Nature Materials**, London, v. 16, n. 1, p. 23–34, 2017.

7 HAQUE, S.; ALEXANDRE, M.; VICENTE, A. T.; LI, K.; SCHUSTER, C. S.; YANG, S.; ÁGUAS, H.; MARTINS, R.; FERREIRA, R. A. S.; MENDES, M. J. Photon shifting and trapping in perovskite solar cells for improved efficiency and stability. **Light: Science & Applications**, London, v. 13, n. 1, p. 238, 2024.

8 HAQUE, S.; ALEXANDRE, M.; BARETZKY, C.; ROSSI, D.; ROSSI, F. D.; VICENTE, A. T.; BRUNETTI, F.; ÁGUAS, H.; FERREIRA, R. A. S.; FORTUNATO, E.; MAUR, M.; WüRFEL, U.; MARTINS, R.; MENDES, M. J. Photonic-structured perovskite solar cells: detailed optoelectronic analysis. **ACS Photonics**, Washington, v. 9, n. 7, p. 2408–2421, 2022.

9 LAKOWICZ, J. R. **Principles of fluorescence spectroscopy**. London: Springer, 2008.

10 CHEN, X.; LIU, Y.; TU, D. **Lanthanide-doped luminescent nanomaterials**. London: Springer, 2016. 1–15 p. ISBN 978-3-319-45197-3.

11 LI, X.; WANG, R.; ZHANG, F.; ZHOU, L.; SHEN, D.; YAO, C.; ZHAO, D. Nd^{3+} sensitized up/down converting dual-mode nanomaterials for efficient in-vitro and in-vivo bioimaging excited at 800 nm. **Scientific Reports**, London, v. 3, n. 1, p. 3536, 2013.

12 ZHOU, L.; ZHENG, X.; GU, Z.; YIN, W.; ZHANG, X.; RUAN, L.; YANG, Y.; HU, Z.; ZHAO, Y. Mesoporous $NaYbF_4$@$NaGdF_4$ core-shell up-conversion nanoparticles for targeted drug delivery and multimodal imaging. **Biomaterials**, Amsterdam, v. 35, n. 26, p. 7666–7678, 2014.

13 ZHANG, W.; ZHANG, X.; SHEN, Y.; SHI, F.; SONG, C.; LIU, T.; GAO, P.; LAN, B.; LIU, M.; WANG, S. *et al.* Ultra-high fret efficiency $NaGdF_4$: Tb^{3+}-rose bengal biocompatible nanocomposite for X-ray excited photodynamic therapy application. **Biomaterials**, Amsterdam, v. 184, p. 31–40, 2018.

14 CHEN, D.; WAN, Z.; ZHOU, Y.; HUANG, P.; ZHONG, J.; DING, M.; XIANG, W.; LIANG, X.; JI, Z. Bulk glass ceramics containing Yb^{3+}/Er^{3+}: β-$NaGdF_4$ nanocrystals: Phase-separation-controlled crystallization, optical spectroscopy and upconverted temperature sensing behavior. **Journal of Alloys and Compounds**, Amsterdam, v. 638, p. 21–28, 2015.

15 NAGPAL, K.; KEDAWAT, G.; SRIVASTAVA, S.; GUPTA, B. K. Luminomagnetic afterglow assimilated multi-mode protection with inventive golden security ink for anticounterfeiting applications. **ACS Applied Materials & Interfaces**, Washington, v. 17, n. 21, p. 31133–31144, 2025.

16 SHRIVER, D. F.; ATKINS, P. **Química inorgânica**. Porto Alegre: Bookman, 2008.

17 GALAÇO, A. R. B. S.; LIMA, J. F.; SERRA, O. A. Os lantanídeos nas redes metalorgânicas: uma nova classe de materiais porosos. **Química Nova**, SciELO Brasil, v. 41, n. 6, 2018.

18 BÜNZLI, J.-C. G.; ELISEEVA, S. V. Basics of lanthanide photophysics. **Lanthanide luminescence: photophysical, analytical and biological aspects**, Springer, p. 1–45, 2010.

19 PARKER, D.; SUTURINA, E. A.; KUPROV, I.; CHILTON, N. F. How the ligand field in lanthanide coordination complexes determines magnetic susceptibility anisotropy, paramagnetic NMR shift, and relaxation behavior. **Accounts of Chemical Research**, Washington, v. 53, n. 8, p. 1520–1534, 2020.

20 BAI, G.; TSANG, M.-K.; HAO, J. Luminescent ions in advanced composite materials for multifunctional applications. **Advanced Functional Materials**, Hoboken, v. 26, n. 35, p. 6330–6350, 2016.

21 RONDA, C.; JÜSTEL, T.; NIKOL, H. Rare earth phosphors: fundamentals and applications. **Journal of Alloys and Compounds**, Amsterdam, v. 275, p. 669–676, 1998.

22 LEI, L.; WANG, Y.; KUZMIN, A.; HUA, Y.; ZHAO, J.; XU, S.; PRASAD, P. N. Next generation lanthanide doped nanoscintillators and photon converters. **ELight**, London, v. 2, n. 1, p. 17, 2022.

23 BOYER, J. C.; CUCCIA, L. A.; CAPOBIANCO, J. A. Synthesis of colloidal upconverting $NaYF_4$:Er^{3+}/Yb^{3+} and Tm^{3+}/Yb^{3+} monodisperse nanocrystals. **Nano Letters**, Washington, v. 7, n. 3, p. 847–852, 2007.

24 YI, G. S.; CHOW, G. M. Synthesis of hexagonal-phase $NaYF_4$:Yb,Er and $NaYF_4$:Yb,Tm nanocrystals with efficient up-conversion fluorescence. **Advanced Functional Materials**, Hoboken, v. 16, n. 18, p. 2324–2329, 2006.

25 CALADO, C. M.; MANALI, Í. F.; DIOGENIS, I. M.; COELHO, S. F.; TEXEIRA, V. C.; MESQUITA, B. R. de; OLIVEIRA, J. L.; SIGOLI, F. A.; REZENDE, M. V. d. S. Defect disorder and optical spectroscopy study of Eu-doped $NaYF_4$ and $NaGdF_4$ nanoparticles. **Optical Materials**, Amsterdam, v. 137, p. 113529, 2023.

26 XU, S.; WANG, W.; ZHANG, Y.; ZHU, S.; TAO, Y.; SONG, H. $NaYF_4$:Yb,Tm nanocrystals and TiO_2 inverse opal composite films: a novel device for upconversion enhancement and solid-based sensing of avidin. **Nanoscale**, London, v. 6, n. 11, 2014.

27 YI, G.-S.; CHOW, G.-M. Water-soluble $NaYF_4$:Yb,Er(Tm)/$NaYF_4$/polymer core/shell/shell nanoparticles with significant enhancement of upconversion fluorescence. **Chemistry of Materials**, Washington, v. 19, n. 3, p. 341–343, 2007.

28 CHEN, S.; PENG, B.; LU, F.; MEI, Y.; CHENG, F.; DENG, L.; XIONG, Q.; WANG, L.; SUN, X.; HUANG, W. Scattering or photoluminescence? Major mechanism exploration on performance enhancement in P3HT-based polymer solar cells with $NaYF_4$:2% Er^{3+},18% Yb^{3+} upconverting nanocrystals. **Advanced Optical Materials**, Hoboken, v. 2, n. 5, p. 442–449, 2014.

29 KONG, M.; HU, W.; CHENG, F.; HUANG, Z.; ZHANG, J.; HAN, Z.; SHI, N.; FAN, Q.; CHEN, S.; HUANG, W. Efficiency enhancement in P3HT-based polymer solar cells with a $NaYF_4$:2%Er^{3+},18%Yb^{3+} up-converter. **Journal of Materials Chemistry C**, London, v. 1, n. 37, p. 5872–5878, 2013.

30 PTACEK, P.; SCHÄFER, H.; KÖMPE, K.; HAASE, M. Crystal phase control of luminescing α-$NaGdF_4$:Eu^{3+} and β-$NaGdF_4$:Eu^{3+} nanocrystals. **Advanced Functional Materials**, Hoboken, v. 17, n. 18, p. 3843–3848, 2007.

31 SHEN, J.; LI, Z.; CHENG, R.; LUO, Q.; LUO, Y.; CHEN, Y.; CHEN, X.; SUN, Z.; HUANG, S. Eu^{3+}-doped -$NaGdF_4$ nanocrystal down-converting layer for efficient dye-sensitized solar cells. **ACS Applied Materials & Interfaces**, Washington, v. 6, n. 20, p. 17454–17462, 2014.

32 BAZIULYTE-PAULAVICIENE, D.; KARABANOVAS, V.; STASYS, M.; JAROCKYTE, G.; PODERYS, V.; SAKIRZANOVAS, S.; ROTOMSKIS, R. Synthesis and functionalization of $NaGdF_4$:Yb,Er@$NaGdF_4$ core–shell nanoparticles for possible application as multimodal contrast agents. **Beilstein Journal of Nanotechnology**, Frankfurt, v. 8, n. 1, p. 1815–1824, 2017.

33 DONG, H.; SUN, L.-D.; YAN, C.-H. Energy transfer in lanthanide upconversion studies for extended optical applications. **Chemical Society Reviews**, London, v. 44, n. 6, p. 1608–1634, 2015.

34 ZHANG, F. **Photon upconversion nanomaterials**. London: Springer, 2015. v. 416.

35 MENG, R.; HE, Z.; LUO, X.; ZHANG, C.; CHEN, M.; LU, H.; YANG, Y. Wide spectral response perovskite solar cells mixed with $NaGdF_4$:Yb^{3+},Er^{3+}@ $NaGdF_4$:Eu^{3+} core-shell rare earth nanoparticles. **Optical Materials**, Amsterdam, v. 119, p. 111326, 2021.

36 LIANG, J.; GAO, H.; YI, M.; SHI, W.; LIU, Y.; ZHANG, Z.; MAO, Y. β-$NaYF_4$:Yb^{3+},Tm^{3+}@TiO_2 core-shell nanoparticles incorporated into the mesoporous layer for high efficiency perovskite solar cells. **Electrochimica Acta**, Amsterdam, v. 261, p. 14–22, 2018.

37 LIU, Y.; TU, D.; ZHU, H.; LI, R.; LUO, W.; CHEN, X. A strategy to achieve efficient dual-mode luminescence of Eu^{3+} in lanthanides doped multifunctional $NaGdF_4$ nanocrystals. **Advanced Materials**, Hoboken, v. 22, n. 30, p. 3266–3271, 2010.

38 KLAMPAFTIS, E.; ROSS, D.; MCINTOSH, K. R.; RICHARDS, B. S. Enhancing the performance of solar cells via luminescent down-shifting of the incident spectrum: a review. **Solar Energy Materials and Solar Cells**, Amsterdam, v. 93, n. 8, p. 1182–1194, 2009.

39 VERMA, D.; SAETRE, T. O.; MIDTGÅRD, O.-M. **Review on Up/Down Conversion Materials for Solar Cell Application**. 2012. 2608–2613 p. 38th IEEE Photovoltaic Specialists Conference (PVSC 2012), Austin, IEEE.

40 SALLEY, G. M.; WENGER, . S.; KRAMER, K. W.; GÜDEL, H. U. Inorganic solid state optical materials: major recent advances. **Current Opinion in Solid State & Materials Science**, Amsterdam, v. 6, p. 487–493, 2002.

41 WEGH, R. T.; DONKER, H.; OSKAM, K. D.; MEIJERINK, A. Visibile quantum cutting in $LiGdF_4$: Eu^{3+} through downconversion. **Science**, Washington, v. 283, n. 5402, p. 663–666, 1999.

42 WANG, H.-Q.; BATENTSCHUK, M.; OSVET, A.; PINNA, L.; BRABEC, C. J. Rare-earth ion doped up-conversion materials for photovoltaic applications. **Advanced Materials**, Hoboken, v. 23, n. 22-23, p. 2675–2680, 2011.

43 BADESCU, V.; BADESCU, A. M. Improved model for solar cells with up-conversion of low-energy photons. **Renewable Energy**, Amsterdam, v. 34, n. 6, p. 1538–1544, 2009.

44 AUZEL, F. Upconversion and anti-stokes processes with *f* and *d* ions in solids. **Chemical reviews**, Washington, v. 104, n. 1, p. 139–174, 2004.

45 WANG, N.; ZHUANG, B.; PANG, T.; ZENG, L.; CHEN, D. Recent advances in lanthanide-doped perovskite nanocrystals. **Laser & Photonics Reviews**, Hoboken, v. 19, n. 10, p. e00905, 2025.

46 ZHONG, Y.; MA, Z.; ZHU, S.; YUE, J.; ZHANG, M.; ANTARIS, A. L.; YUAN, J.; CUI, R.; WAN, H.; ZHOU, Y. *et al.* Boosting the down-shifting luminescence of rare-earth nanocrystals for biological imaging beyond 1500 nm. **Nature communications**, London, v. 8, n. 1, p. 737, 2017.

47 JING, Y.; LOW, A. K.; LIU, Y.; FENG, M.; LIM, J. W. M.; LOH, S. M.; REHMAN, Q.; BLUNDEL, S. A.; MATHEWS, N.; HIPPALGAONKAR, K. *et al.* Stable and highly emissive infrared Yb-doped perovskite quantum cutters engineered by machine learning. **Advanced Materials**, Hoboken, v. 36, n. 44, p. 2405973, 2024.

48 TIMMERMAN, D.; IZEDDIN, I.; STALLINGA, P.; YASSIEVICH, I.; GREGORKIEWICZ, T. Space-separated quantum cutting with silicon nanocrystals for photovoltaic applications. **Nature Photonics**, London, v. 2, n. 2, p. 105–109, 2008.

49 ENDE, B. M. V. D.; AARTS, L.; MEIJERINK, A. Near-infrared quantum cutting for photovoltaics. **Advanced Materials**, Hoboken, v. 21, n. 30, p. 3073–3077, 2009.

50 JOUBERT, M.-F. Photon avalanche upconversion in rare earth laser materials. **Optical Materials**, Amsterdam, v. 11, n. 2-3, p. 181–203, 1999.

51 MEIJERINK, A.; RABOUW, F. T. Giant photon avalanches observed in nanoparticles. **Nature**, London, 2021.

52 AUZEL, F. Upconversion processes in coupled ion systems. **Journal of Luminescence**, Amsterdam, v. 45, n. 1-6, p. 341–345, 1990.

53 REDDY, K. L.; BALAJI, R.; KUMAR, A.; KRISHNAN, V. Lanthanide doped near infrared active upconversion nanophosphors: fundamental concepts, synthesis strategies, and technological applications. **Small**, Hoboken, v. 14, n. 37, p. 1801304, 2018.

54 NUR-E-ALAM, M.; ISLAM, M. S.; ABEDIN, T.; ISLAM, M. A.; YAP, B. K.; KIONG, T. S.; DAS, N.; RAHMAN, M. R.; KHANDAKER, M. U. Current scenario and future trends on stability issues of perovskite solar cells: a mini review. **Current Opinion in Colloid & Interface Science**, Amsterdam, p. 101895, 2025.

55 BASUMATARY, P.; KUMARI, J.; AGARWAL, P. Enhancing the performance and stability of $MAPbI_3$ perovskite solar cells by inserting the ito layer before the ag electrode. **AIP Conference Proceedings**, v. 2369, n. 1, p. 020022, 2021.

56 YANG, H.; WANG, H.; ZHANG, J.; CHANG, J.; ZHANG, C. A facile way to improve the performance of perovskite solar cells by toluene and diethyl ether mixed anti-solvent engineering. **Coatings**, Basel, v. 9, n. 11, p. 766, 2019.

57 HE, C.; ZHANG, F.; ZHAO, X.; LIN, C.; YE, M. Interface engineering of BCP buffer layers in planar heterojunction perovskite solar cells with NiO_x hole transporting layers. **Frontiers in Physics**, Frontiers Media SA, v. 6, p. 99, 2018.

58 DEWI, H. A.; LI, J.; ERDENEBILEG, E.; WANG, H.; BASTIANI, M. D.; WOLF, S. D.; MATHEWS, N.; MHAISALKAR, S.; BRUNO, A. Efficient bandgap widening in co-evaporated $MAPbI_3$ perovskite. **Sustainable Energy & Fuels**, London, v. 6, n. 10, p. 2428–2438, 2022.

59 DUBOSE, J. T.; KAMAT, P. V. Energy versus electron transfer: managing excited-state interactions in perovskite nanocrystal–molecular hybrids: focus review. **Chemical Reviews**, Washington, v. 122, n. 15, p. 12475–12494, 2022.

60 LIN, Y.-R.; LIAO, Y.-S.; HSIAO, H.-T.; CHEN, C.-P. Two-step annealing of NiO_x enhances the NiO_x–perovskite interface for high-performance ambient-stable p–i–n perovskite solar cells. **Applied Surface Science**, Amsterdam, v. 504, p. 144478, 2020.

61 SHOCKLEY, W.; QUEISSER, H. Detailed balance limit of efficiency of p-n junction solar cells. **Journal of Applied Physics**, v. 32, p. 510–519, 1961.

62 BARTESAGHI, D.; Del Carmen Pérez, I.; KNIEPERT, J.; ROLAND, S.; TURBIEZ, M.; NEHER, D.; KOSTER, L. J. A. Competition between recombination and extraction of free charges determines the fill factor of organic solar cells. **Nature Communications**, p. 7083, 2015.

63 GARCIA-BELMONTE, G.; BISQUERT, J. Open-circuit voltage limit caused by recombination through tail states in bulk heterojunction polymer-fullerene solar cells. **Applied Physics Letters**, v. 96, p. 113301, 2010.

64 MULLER, J.; RECH, B.; SPRINGER, J.; VANECEK, M. TCO and light trapping in silicon thin film solar cells. **Solar Energy**, v. 77, p. 917–930, 2004.

65 SINGH, P.; RAVINDRA, N. M. Analysis of series and shunt resistance in silicon solar cells using single and double exponential models. **Emerging Materials Research**, v. 1, p. 33–38, 2002.

66 DAY, J.; SENTHILARASU, S.; MALLICK, T. K. Improving spectral modification for applications in solar cells: a review. **Renewable Energy**, v. 132, p. 186–205, 2019.

67 LI, H.; CHEN, C.; JIN, J.; BI, W.; ZHANG, B.; CHEN, X.; XU, L.; LIU, D.; DAI, Q.; SONG, H. Near-infrared and ultraviolet to visible photon conversion for full spectrum response perovskite solar cells. **Nano Energy**, Amsterdam, v. 50, p. 699–709, 2018.

68 MENG, F.-L.; WU, J.-J.; ZHAO, E.-F.; ZHENG, Y.-Z.; HUANG, M.-L.; DAI, L.-M.; TAO, X.; CHEN, J.-F. High-efficiency near-infrared enabled planar perovskite solar cells by embedding upconversion nanocrystals. **Nanoscale**, London, v. 9, n. 46, p. 18535–18545, 2017.

69 SEBAG, M. S.; HU, Z.; LIMA, K. de O.; XIANG, H.; GREDIN, P.; MORTIER, M.; BILLOT, L.; AIGOUY, L.; CHEN, Z. Microscopic evidence of upconversion-induced near-infrared light harvest in hybrid perovskite solar cells. **ACS Applied Energy Materials**, Washington, v. 1, n. 8, p. 3537–3543, 2018.

70 WU, J.; WEI, S.; WENG, X.; WANG, R.; ZHOU, H.; CHENG, S. Understanding the efficiency enhancement of perovskite solar cells with $NaGdF_4$:Er^{3+}/Yb^{3+} nanorods. **Solar Energy Materials and Solar Cells**, Amsterdam, v. 248, p. 112029, 2022.

71 HU, J.; QIAO, Y.; YANG, Y.; ZHAO, L.; LIU, W.; LI, S.; LIU, P.; CHEN, M. Enhanced performance of hole-conductor-free perovskite solar cells by utilization of core/shell-structured β-NaYF4: Yb^{3+}, Er^{3+}@ SiO_2 nanoparticles in ambient air. **IEEE Journal of Photovoltaics**, New York, v. 8, n. 1, p. 132–136, 2017.

72 ALOTAIBI, A.; ALSARDI, F.; ALSHWIKHAT, F.; ALDOSSARY, M.; ALMARWANI, F. S.; TALIDI, F. J.; ALMENHALI, S. A.; ALMOTAWA, S. F.; ALZAHRANI, Y. A.; ALENZI, S.; ALANAZI, A.; ALKAHTANI, M. Fabrication of erbium-doped upconversion nanoparticles and carbon quantum dots for efficient perovskite solar cells. **Molecules**, Basel, v. 29, n. 11, p. 2556, 2024.

73 OSMAN, M. M.; ALANAZI, A. Q.; ALANAZI, T. I.; ALKAHTANI, M. H.; EL-NAGGAR, A. M.; ALBASSAM, A. A.; ALDHAFIRI, A. M.; AL-GAWATI, M.; ALMALKI, M.; ALENZI, S. M.; MENSI, M. D. Enhanced performance of perovskite solar cell via up-conversion $YLiF_4$: Yb, Er nanoparticles. **Solar Energy Materials and Solar Cells**, Amsterdam, v. 273, p. 112955, 2024.

74 XU, F.; SUN, Y.; GAO, H.; JIN, S.; ZHANG, Z.; ZHANG, H.; PAN, G.; KANG, M.; MA, X.; MAO, Y. High-performance perovskite solar cells based on $NaCsWO_3$@ $NaYF_4$@$NaYF_4$:Yb,Er upconversion nanoparticles. **ACS Applied Materials & Interfaces**, Washington, v. 13, n. 2, p. 2674–2684, 2021.

75 LI, X.; ZHANG, F.; ZHAO, D. Lab on upconversion nanoparticles: optical properties and applications engineering via designed nanostructure. **Chemical Society Reviews**, London, v. 44, n. 6, p. 1346–1378, 2015.

76 LI, Z.; ZHANG, Y. An efficient and user-friendly method for the synthesis of hexagonal-phase $NaYF_4$:Yb,Er/Tm nanocrystals with controllable shape and upconversion fluorescence. **Nanotechnology**, Bristol, v. 19, n. 34, p. 345606, 2008.

77 RODRIGUES, E.; GÁLICO, D.; LEMES, M.; BETTINI, J.; NETO, E.; MAZALI, I.; MURUGESU, M.; SIGOLI, F. One pot synthesis and systematic study of the photophysical and magnetic properties and thermal sensing of α and β-phase $NaLnF_4$ and β-phase core@ shell nanoparticles. **New Journal of Chemistry**, London, v. 42, n. 16, p. 13393–13405, 2018.

78 RODRIGUES, E. M.; GÁLICO, D. A.; MAZALI, I. O.; SIGOLI, F. A. Temperature probing and emission color tuning by morphology and size control of upconverting β-$NaYb_{0.67}Gd_{0.30}F_4$:$Tm_{0.015}$:$Ho_{0.015}$ nanoparticles. **Methods and Applications in Fluorescence**, Bristol, v. 5, n. 2, p. 024012, 2017.

79 ALISHAH, H. M.; CHOI, F. P. G.; MENDA, U. D.; KAHVECI, C.; RODOP, M. C.; MENDES, M. J.; GUNES, S. Effect of bathocuproine concentration on the photovoltaic performance of NiO_x-based perovskite solar cells. **Journal of the Mexican Chemical Society**, Mexico City, v. 65, n. 2, p. 149–160, 2021.

80 ERDENEBILEG, E.; TIWARI, N.; KOSASIH, F. U.; DEWI, H. A.; JIA, L.; MATHEWS, N.; MHAISALKAR, S.; BRUNO, A. Co-evaporated pin perovskite solar cells with sputtered NiO_x hole transport layer. **Materials Today Chemistry**, Amsterdam, v. 30, p. 101575, 2023.

81 AKALIN, S. A.; EROL, M.; UZUNBAYIR, B.; OGUZLAR, S.; YILDIRIM, S.; CHOI, F. P. G.; GUNES, S.; MENDA, U. D. Y.; MENDES, M. J. Physically-deposited hole transporters in perovskite PV: NiO_x improved with Li/Mg doping. **Advanced Materials Technologies**, Hoboken, v. 9, n. 7, p. 2301760, 2024.

82 PALÁCIO, M. P. S.; SANTOS, L. P. M.; BARROS, L. C. E.; OLIVEIRA, N.; COELHO, S. F. N.; COIMBRA, E. A. C.; CAMILO, D. P.; LIMA, F. A. S.; MATURI, F. E.; MENDA, U. D.; SIGOLI, F. A.; SILVA, W. F.; JACINTO, C.; ANDRE, P.; MENDES, M. J.; FERREIRA, R. A. S.; VASCONCELOS, I. F. Dual spectral matching in perovskite solar cells via upconverting plus downshifting nanoparticles. **ACS Applied Energy Materials**, Washington, v. 8, n. 19, p. 14881–14892, 2025.

83 KRÄMER, K. W.; BINER, D.; FREI, G.; GÜDEL, H. U.; HEHLEN, M. P.; LÜTHI, S. R. Hexagonal sodium yttrium fluoride based green and blue emitting upconversion phosphors. **Chemistry of materials**, Washington, v. 16, n. 7, p. 1244–1251, 2004.

84 BIJU, S.; HARRIS, M.; ELST, L. V.; WOLBERG, M.; KIRSCHHOCK, C.; PARAC-VOGT, T. N. Multifunctional β-$NaGdF_4$: Ln^{3+}(Ln= Yb, Er, Dy) nanoparticles with nir to visible upconversion and high transverse relaxivity: a potential bimodal contrast agent for high-field mri and optical imaging. **RSC Advances**, London, v. 6, n. 66, p. 61443–61448, 2016.

85 do Nascimento, J. P. C.; SALES, A. J. M.; SOUSA, D. G.; SILVA, M. A. S. da; MOREIRA, S. G. C.; PAVANI, K.; SOARES, M. J.; GRAÇA, M. P. F.; KUMAR, J. S.; SOMBRA, A. S. B. Temperature-, power-, and concentration-dependent two and three photon upconversion in Er^{3+}/Yb^{3+} co-doped lanthanum ortho-niobate phosphors. **RSC advances**, London, v. 6, n. 72, p. 68160–68169, 2016.

86 LI, Y.; WEI, X.; YIN, M. Synthesis and upconversion luminescent properties of Er^{3+} doped and Er^{3+}-Yb^{3+} codoped GdOCl powders. **Journal of Alloys and Compounds**, Amsterdam, v. 509, n. 41, p. 9865–9868, 2011.

87 HE, S.; XIA, H.; ZHANG, J.; ZHU, Y.; CHEN, B. Highly efficient up-conversion luminescence in Er^{3+}/Yb^{3+} co-doped $Na_5Lu_9F_{32}$ single crystals by vertical bridgman method. **Scientific Reports**, London, v. 7, n. 1, p. 8751, 2017.

88 SOARES, A. C. C.; REGO-FILHO, F. G.; BUENO, L. A.; GOUVEIA-NETO, A. S. Energy-transfer Er^{3+} to Eu^{3+} and frequency upconversion visible emission in $PbGeO_3$: PbF_2: CdF_2 glass. **Chemical Physics Letters**, Amsterdam, v. 706, p. 367–370, 2018.

89 SHEN, S.; RICHARDS, B.; JHA, A. Enhancement in pump inversion efficiency at 980 nm in Er^{3+}, Er^{3+}/Eu^{3+} and Er^{3+}/Ce^{3+} doped tellurite glass fibers. **Optics Express**, Washington, v. 14, n. 12, p. 5050–5054, 2006.

90 DWIVEDI, Y.; RAI, A.; RAI, S. Energy transfer in Er: Eu: Yb co-doped tellurite glasses: Yb as enhancer and quencher. **Journal of Luminescence**, Amsterdam, v. 129, n. 6, p. 629–633, 2009.

91 POLLNAU, M.; GAMELIN, D. R.; LÜTHI, S.; GÜDEL, H.; HEHLEN, M. P. Power dependence of upconversion luminescence in lanthanide and transition-metal-ion systems. **Physical Review B**, College Park, v. 61, n. 5, p. 3337, 2000.

92 VELÁZQUEZ, J. J.; MOSA, J.; GORNI, G.; BALDA, R.; FERNÁNDEZ, J.; PASCUAL, L.; DURÁN, A.; CASTRO, Y. Transparent SiO_2-GdF_3 sol-gel nano-glass ceramics for optical applications. **Journal of Sol-Gel Science and Technology**, London, v. 89, p. 322–332, 2019.

93 YOU, F.; HUANG, S.; LIU, S.; TAO, Y. VUV excited luminescence of $MGdF_4$: Eu^{3+} (M= Na, K, NH_4). **Journal of Luminescence**, Amsterdam, v. 110, n. 3, p. 95–99, 2004.

94 CHEN, C.; WU, Y.; LIU, L.; GAO, Y.; CHEN, X.; BI, W.; CHEN, X.; LIU, D.; DAI, Q.; SONG, H. Interfacial engineering and photon downshifting of $CsPbBr_3$ nanocrystals for efficient, stable, and colorful vapor phase perovskite solar cells. **Advanced Science**, Hoboken, v. 6, n. 11, p. 1802046, 2019.

95 WILHELM, S. Perspectives for upconverting nanoparticles. **ACS Nano**, Washington, v. 11, n. 11, p. 10644–10653, 2017.

96 DATT, R.; BISHNOI, S.; HUGHES, D.; MAHAJAN, P.; SINGH, A.; GUPTA, R.; ARYA, S.; GUPTA, V.; TSOI, W. C. Downconversion materials for perovskite solar cells. **Solar RRL**, Hoboken, v. 6, n. 8, p. 2200266, 2022.

97 QIU, Q.; LIU, H.; QIN, Y.; REN, C.; SONG, J. Efficiency enhancement of perovskite solar cells based on Al_2O_3-passivated nano-nickel oxide film. **Journal of Materials Science**, London, v. 55, p. 13881–13891, 2020.

98 CAO, Y.; STAVRINADIS, A.; LASANTA, T.; SO, D.; KONSTANTATOS, G. The role of surface passivation for efficient and photostable PbS quantum dot solar cells. **Nature Energy**, London, v. 1, n. 4, p. 1–6, 2016.

99 CHEN, P.; YIN, X.; QUE, M.; YANG, Y.; QUE, W. TiO_2 passivation for improved efficiency and stability of ZnO nanorods based perovskite solar cells. **RSC Advances**, London, v. 6, n. 63, p. 57996–58002, 2016.

100 LEE, H.; LI, D. Surface passivation to improve the performance of perovskite solar cells. **Energies**, Basel, v. 17, n. 21, p. 5282, 2024.

101 YANG, W. S.; PARK, B.-W.; JUNG, E. H.; JEON, N. J.; KIM, Y. C.; LEE, D. U.; SHIN, S. S.; SEO, J.; KIM, E. K.; NOH, J. H.; SEOK, S. I. Iodide management in formamidinium-lead-halide–based perovskite layers for efficient solar cells. **Science**, Washington, v. 356, n. 6345, p. 1376–1379, 2017.

102 BI, W.; WU, Y.; CHEN, C.; ZHOU, D.; SONG, Z.; LI, D.; CHEN, G.; DAI, Q.; ZHU, Y.; SONG, H. Dye sensitization and local surface plasmon resonance-enhanced upconversion luminescence for efficient perovskite solar cells. **ACS Applied Materials & Interfaces**, Washington, v. 12, n. 22, p. 24737–24746, 2020.

103 ZHOU, R.; LU, X.; YANG, Q.; WU, P. Nanocrystals for large stokes shift-based optosensing. **Chinese Chemical Letters**, Amsterdam, v. 30, n. 10, p. 1843–1848, 2019.

104 GAVRILUTA, A.; FIX, T.; NONAT, A.; SLAOUI, A.; GUILLEMOLES, J.-F.; CHARBONNIÈRE, L. J. Tuning the chemical properties of europium complexes as downshifting agents for copper indium gallium selenide solar cells. **Journal of Materials Chemistry A**, London, v. 5, n. 27, p. 14031–14040, 2017.

105 SOLODOVNYK, A.; HOLLMANN, A.; OSVET, A.; FORBERICH, K.; STERN, E.; BATENTSCHUK, M.; TAYLOR, R. K.; BRABEC, C. J. Luminescent down-shifting layers with Eu^{2+} and Eu^{3+} doped strontium compound particles for photovoltaics. **Proceedings of SPIE**, California, v. 9178, p. 917806, 2014.

106 PARIMALA, M.; RAO, M.; MURTHY, K.; DUBEY, V. Structural and photoluminescence studies of lithium calcium silicate phosphor doped with Eu^{3+} ion for led application. **Journal of Materials Science: Materials in Electronics**, London, v. 34, n. 19, p. 1486, 2023.

107 LIU, H.; WANG, T.; ZHANG, L.; LI, L.; WANG, Y. A.; WANG, C.; SU, Z. Selected-control fabrication of multifunctional fluorescent–magnetic core–shell and yolk–shell hybrid nanostructures. **Chemistry–A European Journal**, Hoboken, v. 18, n. 12, p. 3745–3752, 2012.

108 WANG, X.; CHANG, H.; XIE, J.; ZHAO, B.; LIU, B.; XU, S.; PEI, W.; REN, N.; HUANG, L.; HUANG, W. Recent developments in lanthanide-based luminescent probes. **Coordination Chemistry Reviews**, Amsterdam, v. 273, p. 201–212, 2014.

109 SYAMCHAND, S.; SONY, G. Europium enabled luminescent nanoparticles for biomedical applications. **Journal of Luminescence**, Amsterdam, v. 165, p. 190–215, 2015.

110 HEFFERN, M. C.; MATOSZIUK, L. M.; MEADE, T. J. Lanthanide probes for bioresponsive imaging. **Chemical Reviews**, Washington, v. 114, n. 8, p. 4496–4539, 2014.

111 KANG, S.; GUO, C.; MA, C.; MU, H.; LIU, Z.; SUN, L. Assessment of the biotoxicity of lanthanides (La, Ce, Gd, and Ho) on zebrafish (danio rerio) in different water environments. **Ecotoxicology and Environmental Safety**, Amsterdam, v. 246, p. 114169, 2022.

112 ZHENG, S.; CHEN, W.; TAN, D.; ZHOU, J.; GUO, Q.; JIANG, W.; XU, C.; LIU, X.; QIU, J. Lanthanide-doped $NaGdF_4$ core–shell nanoparticles for non-contact self-referencing temperature sensors. **Nanoscale**, London, v. 6, n. 11, p. 5675–5679, 2014.

113 HAQUE, E.; WARD, A. C. Zebrafish as a model to evaluate nanoparticle toxicity. **Nanomaterials**, Basel, v. 8, n. 7, p. 561, 2018.

114 ASHARANI, P. V.; WU, Y. L.; GONG, Z.; VALIYAVEETTIL, S. Toxicity of silver nanoparticles in zebrafish models. **Nanotechnology**, Bristol, v. 19, n. 25, p. 255102, 2008.

115 SALES, T. O.; CHAVES, J. M.; JACINTO, C. Smart and efficient multi-color tuning using fluoride upconversion nanoparticles blending. **Optical Materials: X**, Amsterdam, v. 20, p. 100260, 2023.

116 OECD. **Test No. 236: Fish Embryo Acute Toxicity (FET) Test**. Paris, 2025. 1–26 p.

117 DE MEDEIROS, A. M. Z.; KHAN, L. U.; DA SILVA, G. H.; OSPINA, C. A.; ALVES, O. L.; DE CASTRO, V. L.; MARTINEZ, D. S. T. Graphene oxide-silver nanoparticle hybrid material: an integrated nanosafety study in zebrafish embryos. **Ecotoxicology and Environmental Safety**, Amsterdam, v. 209, p. 111776, 2021.

118 ZUO, X.; CHEN, Y.; TONG, J.; GENG, X.; FU, X.; GAO, S.; CHEN, H. Effect of Si^{4+}/Gd^{3+} doping on luminescence properties of orangish-red light-emitting phosphors of $KBaBP_2O_8$: Eu^{3+}. **Applied Physics A**, London, v. 128, n. 10, p. 886, 2022.

119 LIU, Y.; ZHOU, S.; ZHUO, Z.; LI, R.; CHEN, Z.; HONG, M.; CHEN, X. In vitro upconverting/downshifting luminescent detection of tumor markers based on Eu^{3+}-activated core–shell–shell lanthanide nanoprobes. **Chemical Science**, London, v. 7, n. 8, p. 5013–5019, 2016.

120 ZHU, X.; TIAN, S.; CAI, Z. Toxicity assessment of iron oxide nanoparticles in zebrafish (danio rerio) early life stages. **PLOS One**, Public Library of Science, 2012.

121 VICARIO-PARÉS, U.; CASTAÑAGA, L.; LACAVE, J. M.; ORON, M.; REIP, P.; BERHANU, D.; VALSAMI-JONES, E.; CAJARAVILLE, M. P.; ORBEA, A. Comparative toxicity of metal oxide nanoparticles (CuO, ZnO and TiO_2) to developing zebrafish embryos. **Journal of Nanoparticle Research**, London, v. 16, n. 8, p. 2550, 2014.

APPENDIX A – EVALUATION OF DOWNSHIFTING PROPERTIES AND TOXICITY OF $NaGdF_4:Eu^{3+}$ NANOPARTICLES IN ZEBRAFISH

A.1 Introduction

Nanoparticles doped with rare earth elements, such as trivalent europium (Eu^{3+}), exhibit exceptional photophysical properties, including a pronounced Stokes shift, which enhances the performance of biodetection techniques by preventing the reabsorption of emitted light (103). This phenomenon, known as downshifting, involves the absorption of high-energy photons by the material, followed by a relaxation process in which the absorbed energy is dissipated through non-radiative transitions (9). These transitions typically involve vibrational relaxation or interactions with phonons, leading to the emission of lower-energy photons, often in the visible or near-infrared range (33). The Stokes shift arises from the energy difference between the absorbed high-energy photons (e.g., ultraviolet or blue light) and the emitted photons of lower energy, usually in the visible or near-infrared regions. The efficiency of this process depends on the specific energy levels of dopant ions, such as Eu^{3+}, which facilitate transitions between excited and ground states (104–106). Lower-energy photons, particularly in the near-infrared (NIR) region, are advantageous for biomedical applications due to their greater tissue penetration and reduced autofluorescence, leading to improved contrast in biological imaging (107). Such materials also display sharp emission peaks with narrow bandwidths (108), low susceptibility to photobleaching, high photochemical stability, low toxicity, and minimal blinking (109, 110).

Rare-earth-doped nanoparticles are attractive for biomedical applications, including biosensors, biotagging, and imaging (111). In addition to providing sharp and intense emission, downshifting materials improve the signal-to-noise ratio in imaging systems, as their lower-energy emissions minimize interference from autofluorescence in biological samples. This unique optical behavior renders these materials ideal for applications requiring high brightness and spectral precision, such as optoelectronic devices, imaging agents, and diagnostic tools.

Although the photoluminescent properties of $NaGdF_4:Eu^{3+}$ nanoparticles are well documented, toxicity evaluation is crucial for determining their safety profile in biomedical applications (31, 92, 112). Recent studies indicate that rare earth elements are significantly enriched in soils and plants near mining areas, with rising concentrations also observed in aquatic ecosystems (111). Toxicity concerns primarily stem from the potential release of free rare earth ions, which may interact with cellular components and cause adverse biological effects. To

address these issues, the zebrafish (*Danio rerio*) has been widely adopted as a model for assessing nanoparticle toxicity due to its transparent embryos, rapid development, and well-characterized genetic background (113, 114). These features allow real-time monitoring of nanoparticle uptake, distribution, and potential toxic effects at both cellular and organismal levels. Moreover, the physiological similarities between zebrafish and higher vertebrates provide valuable insights into the biological compatibility of nanomaterials (110).

In this study, we investigate the downshifting properties and toxicity of $NaGdF_4:Eu^{3+}$ nanoparticles, combining advanced photoluminescence characterization with toxicological evaluation in zebrafish. By integrating these approaches, we aim to bridge the gap between the promising optical properties of $NaGdF_4:Eu^{3+}$ nanoparticles and their biological safety.

A.2 Experimental Procedure

A.2.1 Materials

Gadolinium(III) chloride ($GdCl_3$, 99.9%), europium(III) chloride ($EuCl_3$, 99.9%), ammonium fluoride (NH_4F, 99.99%), and sodium hydroxide (NaOH, ≥97.0%) were purchased from Sigma-Aldrich. Ethylene glycol ($C_2H_6O_2$, 99.0%) was obtained from Merck. All chemicals were of analytical grade and used as received without further purification. Wild-type zebrafish (*Danio rerio*) embryos at 3 h post-fertilization (hpf) were used for all *in vivo* toxicity assays.

A.2.2 Synthesis of $NaGdF_4:Eu^{3+}$ Nanoparticles

The $NaGdF_4:Eu^{3+}$ nanoparticles were synthesized via a co-precipitation method adapted from Sales *et al.*(2023) (115). Briefly, a precursor solution was prepared by dissolving 120 mg of NaOH, 327.10 mg of $GdCl_3$, and 150 mg of $EuCl_3$ in 30 mL of ethylene glycol under vigorous stirring. Separately, 162.98 mg of NH_4F was dissolved in 20 mL of ethylene glycol. The fluoride solution was heated to and maintained at 80 °C under continuous stirring (360 rpm). The NaOH solution was first added to the heated fluoride solution. After 10 minutes, the gadolinium solution was introduced, followed by the addition of the europium solution 10 minutes later. The resulting mixture was stirred for 2 h at 80 °C. The precipitate was then cooled to room temperature, collected by centrifugation at 6000 rpm for 10 minutes, and washed three times with deionized water. The final product was dried at 80 °C for 48 h, ground to a fine, whitish powder in an agate mortar, and stored in a vacuum desiccator to prevent moisture absorption.

A.2.3 Zebrafish Embryo Toxicity Testing

The toxicity of the nanoparticles was evaluated using the zebrafish embryo acute toxicity (FET) test following OECD guideline 236 (116). Wild-type zebrafish (*Danio rerio*) embryos at 3 hours post-fertilization (hpf) were selected based on viability under a stereomicroscope. Only embryos exhibiting normal development were used; those with delayed development, abnormalities, or coagulation were discarded. Selected embryos (n = 24 per concentration) were individually exposed to 2 mL of test solution in 24-well plates. The test solutions consisted of a control (standard reconstituted water) and a range of $NaGdF_4:Eu^{3+}$ nanoparticle concentrations (12.5, 25, 50, and 100 $mg{\cdot}L^{-1}$). The exposure plates were maintained in a climate-controlled chamber at 28.0 ± 0.2 °C under a 14/10 h light/dark cycle for 96 h. Test solutions were renewed daily. Embryos and larvae were examined every 24 h to record mortality and observe malformations. At the end of the 96 h exposure, surviving larvae (n = 10 per group) were anesthetized, photographed, and measured for total length. The lethal concentration for 50% of the embryos (LC_{50}) was calculated based on the mortality data. All experiments were approved and conducted in triplicate. Animal procedures were approved by the Ethics Committee on Animal Use of the Federal University of Ceará (CEUA protocol/ No 4645080322) and followed the methodology described by Medeiros *et al.*(2021) (117).

A.2.4 Characterization Techniques

The synthesized $NaGdF_4:Eu^{3+}$ nanoparticles were characterized using a suite of techniques to determine their structural, morphological, and optical properties.

A.2.4.1 Structural and Morphological Characterization:

The crystal structure and phase purity were analyzed by X-ray diffraction (XRD) using a PANalytical X'Pert MPD powder diffractometer equipped with a Co Kα radiation source (λ = 1.789 Å). Measurements were performed in a 2θ range from 10° to 60° with an operating voltage and current of 40 kV and 45 mA, respectively. Morphology, size distribution, and microstructure were investigated by transmission electron microscopy (TEM) using a Hitachi HD2700 scanning transmission electron microscope (STEM) operated at 200 kV. Samples for TEM analysis were prepared by drop-casting a dilute suspension of nanoparticles in ethanol onto a carbon-coated copper grid and allowing it to dry at room temperature.

A.2.4.1 Optical Characterization:

The photoluminescence properties were studied using a FluoTime 300 spectrofluorometer (PicoQuant GmbH). Emission and excitation spectra were recorded at room temperature (298 K) using a 300 W Xenon arc lamp as the excitation source. The emission was dispersed by an additive monochromator (1200 grooves mm^{-1}, blazed at 500 nm) and detected by a photomultiplier tube (PMA-C 192-N-M, PicoQuant) operating in right-angle geometry. All spectra were acquired with an integration time of 0.5 s and a spectral resolution of 0.5 nm. Emission spectra were corrected for the instrumental response of the detection system, and excitation spectra were corrected for the spectral intensity of the lamp using a built-in reference photodiode. The absolute photoluminescence quantum yield (QY) was measured directly using an integrating sphere apparatus (Hamamatsu Absolute PL Quantum Yield Spectrometer C13534). This system, equipped with a 150 W xenon lamp and a spectrometer, allows for standard-free QY determination by capturing and integrating all emitted photons from a sample excited at a selected wavelength.

A.2.4.1 Biological Imaging:

For the toxicological assessment, bright-field and confocal fluorescence images of zebrafish larvae were acquired using a Zeiss LSM 710 confocal laser scanning microscope. A 405 nm laser diode was used to excite the Eu^{3+} dopant ions, and the resulting emission was collected through a 40x objective (NA = 1.2). Image capture, processing, and three-dimensional reconstruction were performed using the ZEN 2011 software suite.

A.3 Results and Discussion

A.3.1 Structural, Morphological, and Optical Characterization of $NaGdF_4$:Eu^{3+}anoparticles

The structural, morphological, and optical properties of the synthesized β-$NaGdF_4$:Eu^{3+} nanoparticles were comprehensively characterized. The XRD pattern (Fig. 20a) confirms the formation of the pure hexagonal phase (β-phase), as all diffraction peaks are indexed to the reference standard ICDD 00-027-0699 and align with characteristic planes such as (100), (110), and (101) (84). The absence of secondary phases indicates a successful doping process and high phase purity.

Figure 20 – Characterization of $NaGdF_4:Eu^{3+}$ nanoparticles. **(a)** XRD pattern confirming the hexagonal phase by comparison with the reference (ICDD: 00-027-0699). **(b)** TEM image showing morphology and size distribution, with a histogram indicating an average diameter of ~20.5 nm. **(c)** Excitation (left, monitored at 592 nm) and emission (right, excited at 405 nm) spectra, displaying the characteristic Eu^{3+} transitions. **(d)** Schematic energy-level diagram of Eu^{3+}, illustrating absorption at 405 nm ($^7F_0 \rightarrow {}^5L_6$) followed by radiative transitions in the visible range, responsible for the downshifting luminescence.

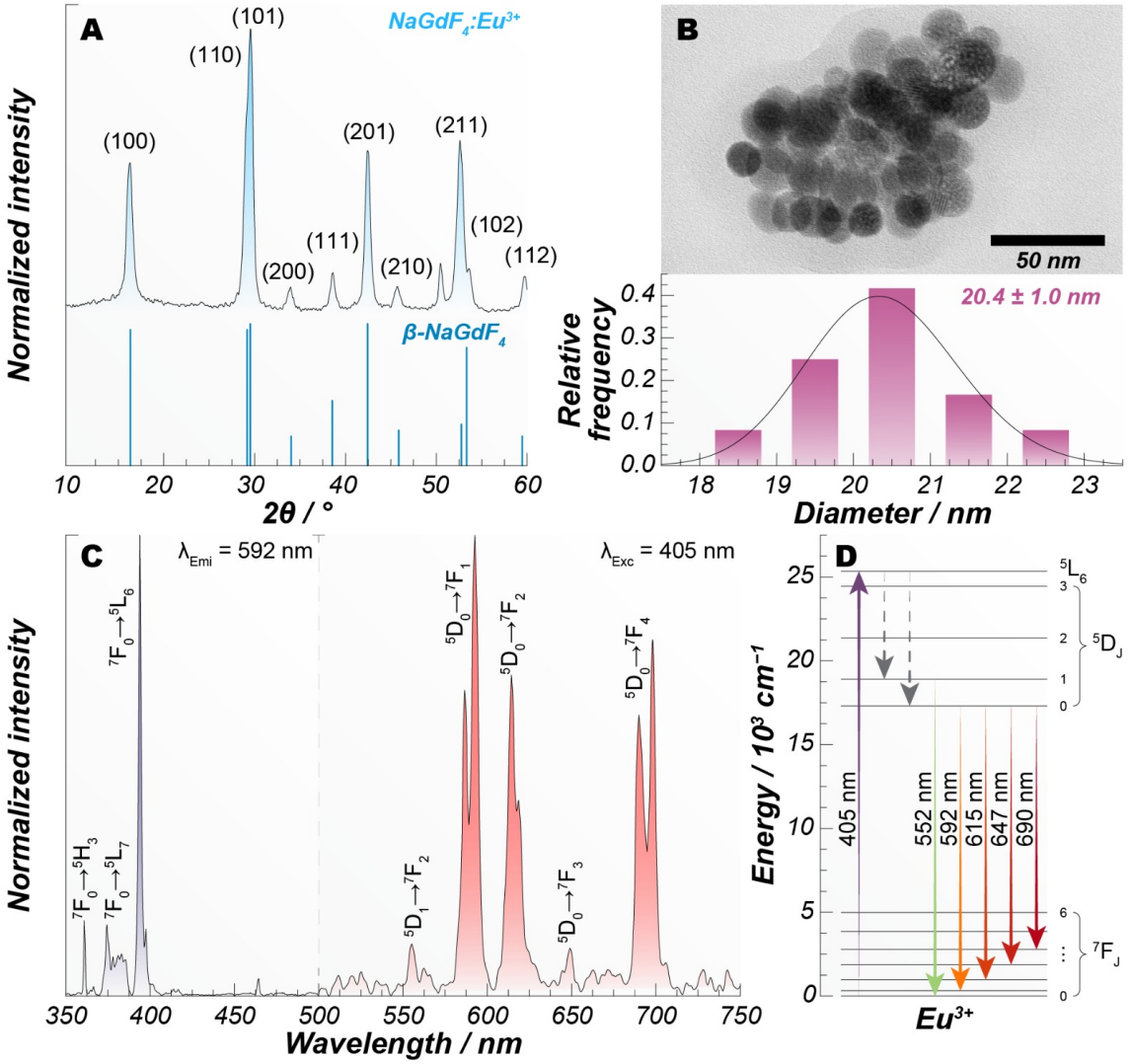

Source: Maturi (2025, unpublished).

TEM analysis (Fig. 20b) reveals nanoparticles with an approximately spherical morphology and a narrow size distribution. The histogram inset yields an average particle diameter of 20.5 ± 1.8 nm, suggesting effective control over nucleation and growth during the co-precipitation synthesis. This monodispersity is crucial for achieving consistent optical properties and predictable biological interactions.

The nanoparticles exhibit characteristic Eu^{3+} downshifting luminescence. The excitation spectrum (Fig. 20c, left), monitored at the $^5D_0 \rightarrow ^7F_1$ transition (592 nm), shows sharp intra-4f transitions of Eu^{3+}, with the most intense peak located at 395 nm ($^7F_0 \rightarrow ^5L_6$) (92, 118). The spectral overlap with a common 405 nm laser is highly advantageous for practical applications. Upon excitation at 405 nm, the emission spectrum (Fig. 20c, right) displays the typical lines of Eu^{3+}, corresponding to transitions from the $^5D_1$ and $^5D_0$ excited states to the ^7F_J (J=0–4) ground state multiplets. The prominent orange emission at 592 nm ($^5D_0 \rightarrow ^7F_1$) is a magnetic dipole transition, whose intensity is largely independent of the crystal field environment (31, 119). The energy-level diagram in Fig. 20d schematically illustrates this downshifting process.

Although energy transfer from Gd^{3+} to Eu^{3+} upon 274 nm excitation results in a higher quantum yield (14.6 ± 1.5%), the 405 nm direct excitation of Eu^{3+} was selected for all *in vivo* studies. Despite its lower quantum yield (6.1 ± 0.6%), this wavelength offers an optimal balance between sufficient signal intensity and minimized photodamage risk to biological samples, ensuring biocompatibility for prolonged imaging of zebrafish embryos.

Having confirmed the desired optical properties, we next evaluated the biological safety of these nanoparticles using the zebrafish model.

A.3.2 In vivo Toxicity Assessment in Zebrafish Embryos

The potential toxicity of the $NaGdF_4$:Eu^{3+} nanoparticles was rigorously evaluated using the zebrafish embryo model according to OECD guidelines (116). Embryos exposed to nanoparticle concentrations up to 100 mg·L^{-1} showed no significant adverse effects compared to the negative control (reconstituted water).

Embryo Viability and Development: The survival rate (Fig. 21a) remained high (~95%) across all NP concentrations after 96 h post-fertilization (hpf), demonstrating a lack of acute toxicity. The hatching rate (Fig. 21b), an indicator of embryonic development, commenced at 48 hpf and reached completion by 72 hpf in all NP-exposed groups, paralleling the control. This indicates that the nanoparticles do not interfere with the critical developmental hatching.

Figure 21 – Toxicity of $NaGdF_4:Eu^{3+}$ nanoparticles in *Danio rerio* embryos. **(a)** Survival rate of embryos exposed to europium nanoparticles. **(b)** Hatching rate of embryos. **(c)** Malformation rate. **(d)** Body length and yolk sac size at 96 hpf.

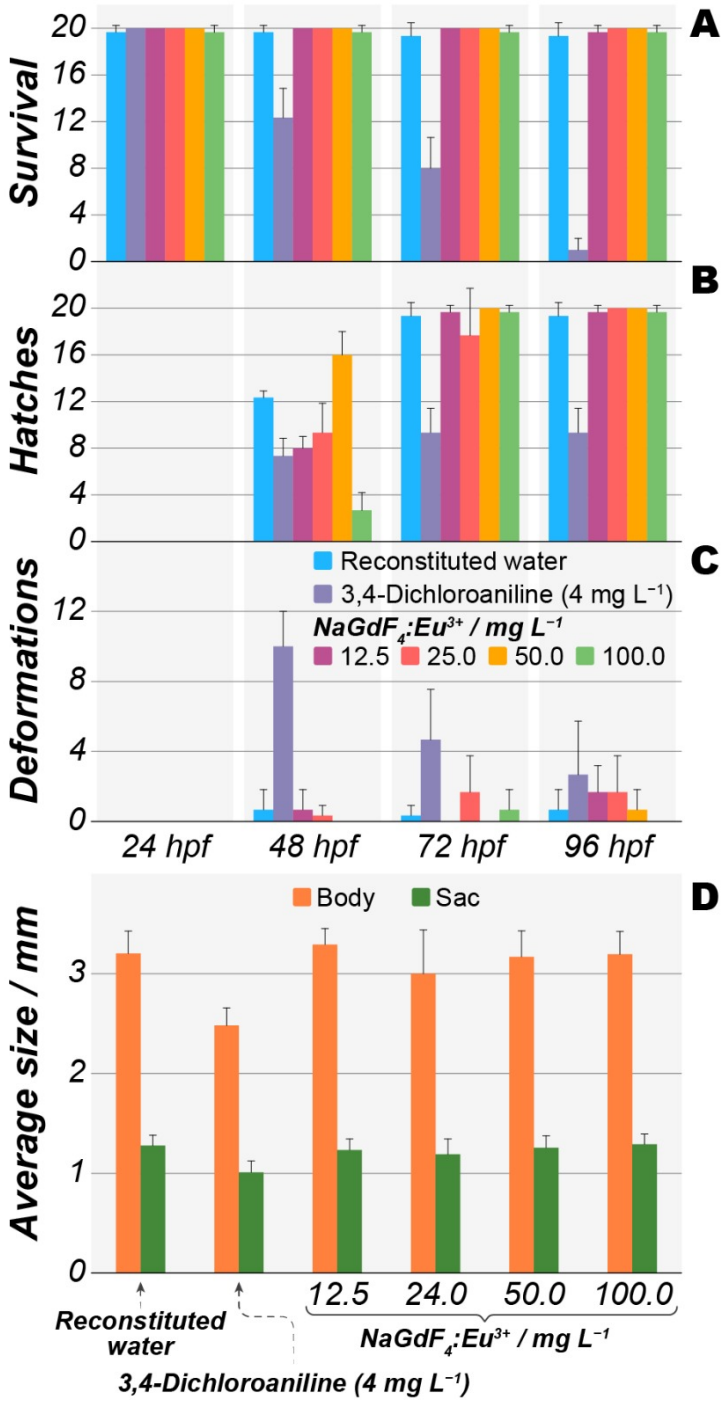

Source: Maturi (2025, unpublished).

Morphological Analysis: Crucially, no significant increase in malformations was observed in any NP-treated group (Fig. 21c). Morphometric analysis of body length and yolk sac size at 96 hpf (Fig. 21d) confirmed normal growth, with all measurements being statistically identical to the control. Brightfield micrographs (Fig. 22E-L) further corroborated these findings, showing normal morphology and the absence of cardiac edema or other deformities, which were prevalent in the positive control (4 mg·L^{-1} dichloroaniline; Fig. 22D).

The observed biocompatibility is notable. Many metallic oxide nanoparticles (e.g., ZnO, CuO) induce significant toxicity at concentrations far below 100 mg·L^{-1}, causing mortality, hatching delays, and malformations (120, 121). The inertness of our $NaGdF_4$:Eu^{3+} nanoparticles suggests effective shielding of the potentially toxic Eu^{3+} ions within the stable $NaGdF_4$ host matrix, preventing ion leaching and subsequent adverse biological interactions.

Figure 22 – (A, C, E, G, I, K) Danio rerio after 24 h exposure. (B, D, F, H, J, L) Danio rerio after 96 h exposure. In (D), note the presence of myocardial edema, a deformation not observed in the other 96 h images. Scale bar: 500 μm (A–L).

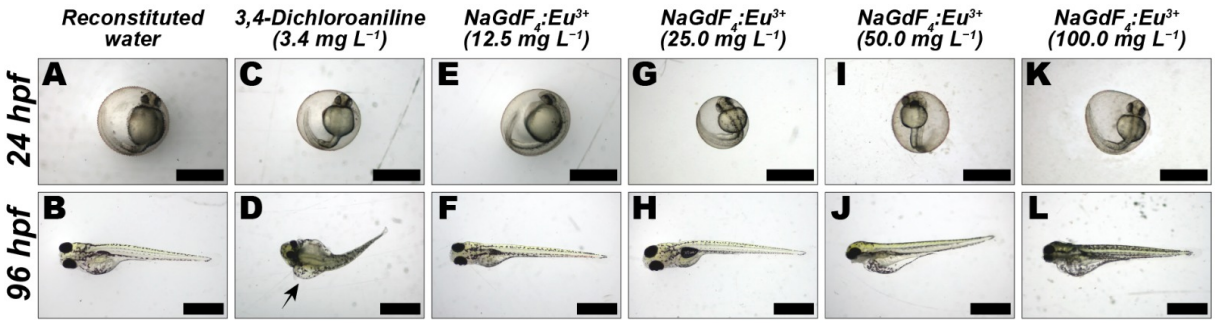

Source: Maturi (2025, unpublished).

A.3.3 Biodistribution and Bioimaging

Confocal laser scanning microscopy was employed to track the biodistribution of the nanoparticles. Embryos incubated without NPs (Fig. 23) exhibited only green autofluorescence ($\lambda_{em} \approx 480$ nm) under 405 nm excitation, with no signal in the red channel (640 nm), confirming the absence of background interference.

Figure 23 – Images of zebrafish embryos without incubation with $NaGdF_4:Eu^{3+}$, acquired at 24 and 96 hpf. Brightfield images display embryo morphology. Fluorescence recorded under 405 nm excitation shows only autofluorescence (at 480 nm) and no emission at 640 nm. Merged images confirm that, in the absence of nanoparticles, no fluorescence is detected in this spectral region.

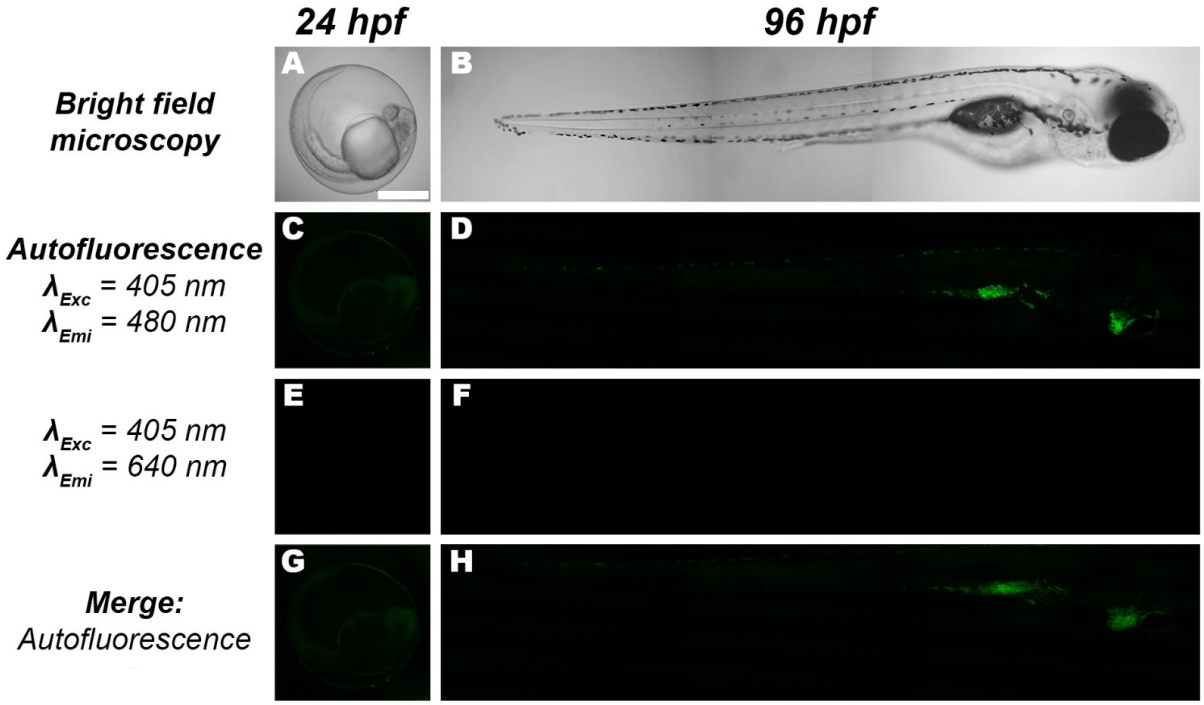

Source: Maturi (2025, unpublished).

In contrast, embryos exposed to $NaGdF_4:Eu^{3+}$ NPs (Fig. 24) exhibited distinct red luminescence (λem = 640 nm, $^5D_0 \rightarrow {}^7F_3$ transition of Eu^{3+}) upon 405 nm excitation. At 24 hpf, the signal was diffuse. By 96 hpf, the red fluorescence was predominantly localized in the intestinal region (Fig. 24F, H), indicating ingestion and internalization of the nanoparticles through normal feeding behavior after hatching. The absence of signal on the chorion confirms that nanoparticles did not merely adhere to the embryo's surface but were taken up internally. Most importantly, this internalization occurred without inducing any observable structural damage or toxicity, as evidenced by the normal morphology in brightfield images (Fig. 24A, B). The merged channels (Fig. 24G, H) clearly colocalize the Eu^{3+} emission with the larval anatomy, demonstrating the effectiveness of these nanoparticles as luminescent biomarkers for *in vivo* imaging. The results of this study will contribute to the development of safer, more effective nanoparticle-based technologies for biomedical applications, particularly in biomarker development, cellular imaging, and targeted therapies. Furthermore, this work highlights the

importance of striking a balance between innovation in nanomaterial design and rigorous safety assessments to ensure their feasibility in real-world applications. These findings reinforce the real possibility of using $NaGdF_4:Eu^{3+}$ nanoparticles as carriers or signal inducers in biological systems.

Figure 24 – Confocal laser scanning microscopy of zebrafish embryos and larvae at 24 and 96 hpf. (A, B) Brightfield images. (C, D) Autofluorescence (emission at 480 nm). (E, F) Europium fluorescence (emission at 640 nm). (G, H) Merged images showing both autofluorescence and europium fluorescence in zebrafish larvae at 24 and 96 hpf. Scale bar: 500 μm.

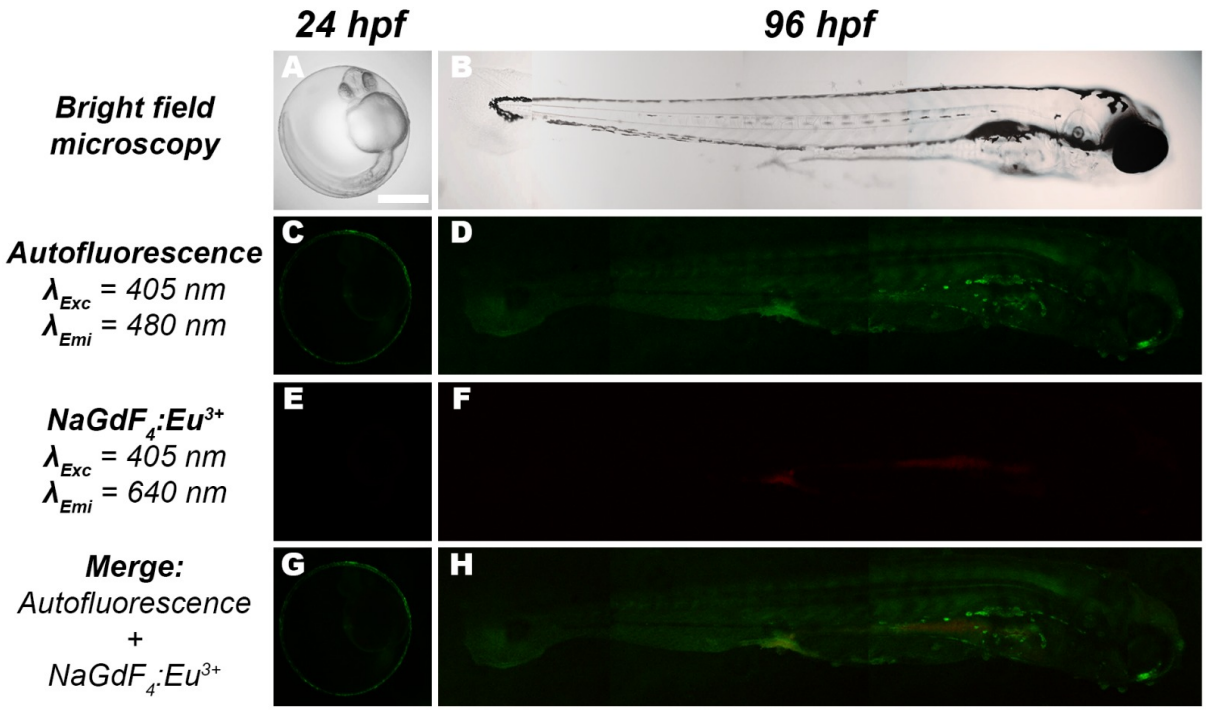

Source: Maturi (2025, unpublished).

A.4 Conclusions

This study demonstrates the synthesis of monodisperse, hexagonal-phase $NaGdF_4:Eu^{3+}$ nanoparticles, which exhibit strong downshifting luminescence characterized by sharp emission peaks typical of Eu^{3+} transitions. The most significant finding is the exemplary biocompatibility of these nanoparticles. A comprehensive toxicological assessment in zebrafish embryos revealed no adverse effects on survival, hatching, morphology, or development at concentrations up to 100 $mg{\cdot}L^{-1}$, a stark contrast to the pronounced toxicity observed in the positive control.

The internalization of the nanoparticles, confirmed via confocal microscopy, occurred without inducing observable structural damage. The biodistribution showed a primary localization in the intestinal region by 96 hpf, indicative of ingestion post-hatching. Crucially, the characteristic red emission of Eu^{3+} upon 405 nm excitation was effectively detected *in vivo*, highlighting the dual functionality of these nanoparticles as both safe and effective luminescent probes for bioimaging.

In conclusion, the combination of promising optical properties, high biocompatibility, and successful performance as an *in vivo* imaging agent underscores the strong potential of $NaGdF_4$:Eu^{3+} nanoparticles for biomedical applications, particularly as fluorescent biomarkers for diagnostic imaging. While acute toxicity was not detected, further investigations are essential to assess long-term effects, potential bioaccumulation, and performance in more complex mammalian systems. This work underscores the importance of balancing innovative nanomaterials design with rigorous safety assessments to ensure their feasibility for real-world biomedical applications.

APPENDIX B – LIST OF PUBLICATIONS

This appendix presents the scientific publications authored or co-authored during the period of doctoral research, comprising peer-reviewed articles, book chapters, and conference proceedings:

1. **Palácio, M. P. S.**; Oliveira, R. N. L.; Resquim, L. S. M.; Lima, F. A. S.; Maturi, F. E.; Ferreira, R. A. S.; Santos, L. P. M.; Miguel, E. C.; Vasconcelos, I. F. Evaluation of Downshifting Properties and Toxicity of $NaGdF_4$:Eu^{3+} Nanoparticles in Zebrafish. *Manuscript in preparation*, 2025.
2. **Palácio, M. P. S.**; Pinheiro, A. G.; Silva, W. Q. N. Crescimento de filmes finos de CdS por CBD. In: Nascimento, A. K. A.; Barboza, F. M. (Org.). **Espaço, tempo e serra: 15 anos ensinando e aprendendo Física na Ibiapaba**. 1. ed. Iguatu, CE: Quipá Editora, 2025, p. 206–216.
3. Medina, L. S. R.; **Palácio, M. P. S.**; Santos, L. P. M.; Vasconcelos, I. F. Multispectral luminescente nanomaterials based on a $NaYF_4$/$NaGdF_4$ matrix. In: XXIII B-MRS Meeting, 2025, Salvador, BA.
4. **Palácio, M. P. S.**; Santos, L. P. M.; Barros, L. C. E.; Oliveira, N.; Coelho, S. F. N.; Coimbra, E. A. C.; Camilo, D. P.; Lima, F. A. S.; Maturi, F. E. M.; Menda, U. D.; Sigoli, F. A.; Silva, W. F.; Jacinto, C.; Andre, P.; Mendes, M. J.; Ferreira, R. A. S.; Vasconcelos, I. F. Dual Spectral Matching in Perovskite Solar Cells via Upconverting plus Downshifting Nanoparticles. **ACS Applied Energy Materials**, 2025. https://doi.org/10.1021/acsaem.5c02611
5. **Palácio, M. P. S.**; Vasconcelos, V. M. R.; Santos, L. P. M.; Salomão, F. C. C. S.; Barros, E. B.; Vasconcelos, I. F. Photoluminescence Suppression in P3HT:PCBM Films Induced by Spinel Ferrite Nanoparticles Decoration. **Journal of Electronic Materials**, 2025. http://dx.doi.org/10.1007/s11664-025-12293-9
6. Oliveira, R. N. L.; **Palacio, M. P. S.**; Carmo, F. F.; Nascimento, J. P. C.; Sales, A. J. M.; Sombra, A. S. B.; Santos, L. P. M.; De Vasconcelos, I. F. . Study of the optical properties of lanthanide-based nanoparticles with energy up and down conversion properties obtained by co-precipitation. In: 25 Congresso Brasileiro de Engenharia e Ciência de Materiais - CBECiMat, 2024, Fortaleza, CE.
7. **Palacio, M. P. S.**; Barros, L. C. E.; Oliveira, N. A.; Coelho, S. F. N.; Lima, F. A. S.; Santos, L. P. M.; Sigoli, F. A.; Silva, W. F.; Silva, C. J.; Vasconcelos, I. F. Advanced Luminescent Nanostructures for Enhanced Solar Cell Applications. In: 25 Congresso Brasileiro de

Engenharia e Ciência de Materiais - CBECiMat, 2024, Fortaleza, CE.

8. **Palacio, M. P. S.**; Oliveira, S. N. C.; Barros, L. C. E.; Oliveira, N. A.; Coelho, S. F. N.; Lima, F. A. S.; Sigoli, F. A.; Silva, W. F.; Silva, C. J.; Vasconcelos, I. F. Optical characterization of $NaGdF_4$-based core-shell nanoparticles with energy upconversion properties. In: XXI B-MRS Meeting, 2023, Maceió, AL.
9. **Palacio, M. P. S.**; Oliveira, S. N. C.; Santos, L. P. M.; Vasconcelos, I. F. Optical properties of hexagonal $NaYF_4$:Yb^{3+},Er^{3+}@$NaYF_4$:Eu^{3+} core-shell nanostructures. In: 3rd (ICAIC) International Conference for Academia and Industry Co-operation & 3rd (IMMSEM) International Meeting in Materials Science and Engineering of Maranhão, 2022, Barreirinhas, MA.
10. Moreira, F. S.; Sarmento, J. S.; Nascimento, L. M.; **Palacio, M. P. S.**; Garcia, P. H. N.; Alves, R. S. G.; Santos, V. S.; Vasconcelos, V. M. R.; Nogueira, R. E. F. Q. Os avanços na técnica de sinterização a frio: redução no consumo de energia e otimização na fabricação de cerâmicas funcionais. In: Lara, N. (Org.). **Engenharia de Materiais: Materializando o Futuro**. 1. ed. São Paulo: Pimenta Cultural, 2022, p. 69–89.
11. Pereira, M. S.; Vasconcelos, V. M. R.; **Palacio, M. P. S.**; Oliveira, F. G. S.; Santos, L. P. M.; Vasconcelos, D. L. M.; Freire, P. T. C.; Vasconcelos, I. F. Characterization of $CoFe_2O_4$, $NiFe_2O_4$, and $ZnFe_2O_4$ nanoparticles synthesized by a proteic sol-gel method. **Journal of Superconductivity and Novel Magnetism**, v. 34, p. 2845–2853, 2021. http://dx.doi.org/10.1007/s10948-021-05968-x